This is to certify that the

thesis entitled

Structure and Energy Absorbing Properties of a Polypropylene and Polyethylene Terephthalate Fiber Composite Material

presented by

Tammy S. Cummings

has been accepted towards fulfillment
of the requirements for

Master's degree in Mechanics

Lawrence T. Drzal
Major professor

Date 9/26/99

STRUCTURE and ENERGY ABSORBING PROPERTIES of a POLYPROPYLENE and POLYETHYLENE TEREPHTHALATE FIBER COMPOSITE MATERIAL

By

Tammy S. Cummings

A THESIS

Submitted to
Michigan State University
in partial fulfillment of the requirements
for the degree of

MASTER OF SCIENCE

Department of Materials Science and Mechanics

1999

ABSTRACT

STRUCTURE and ENERGY ABSORBING PROPERTIES of a POLYPROPYLENE and POLYETHYLENE TEREPHTHALATE FIBER COMPOSITE MATERIAL

By

Tammy S. Cummings

Due to stricter safety standards enforced by the Federal Government, such as FMVSS 201, standards of what is acceptable for automotive interiors are raised to higher levels. As safety and cost become the number one goal of auto manufacturers, materials must be fabricated to meet existing standards, as well as future ones.

One such inhomogeneous material is a polypropylene (PP) and polyethylene terephthalate (PET) energy absorbing material (EAM). This thesis thoroughly investigates measurements of the amount of energy absorbed at various strain rates and impacts, and the effects of processing on material properties such as stiffness. In order to gain an understanding of the morphology and functionality of the material, failure modes were examined at various strain rates and impact speeds through microscopy.

The results of this project show that due to the inhomogeneity of the EAM, a correlation between the way the material functions at various strain rates or impact speeds and the amount of energy it absorbs is difficult to obtain. It also shows that on can change the mechanical properties of the EAM by changing process conditions.

ACKNOWLEDGEMENTS

I would first like to thank two very special people: Brian Erickson and Linda Chamberlain. Without the two of them, this would have never been possible. I would like to thank Linda for giving me inspiration and support for going back to school and getting my Master's Degree. Brian, thank-you so much for being the older brother that I never had. You supported me from beginning to end. You were not only a good boss, but also what a TRUE MENTOR should be, as well as my friend. I thank-you for believing in me when I didn't believe in myself. You will never know how much your support meant to me.

Mother and Father, I thank you both for your continued support and love. I love you both very much. It is because of you that I was able to do this. I dedicate this thesis to the two of you.

I would like to send out a heartfelt thanks to all the guys from my lab who were there to help me out and lend me their support: Phil Culcasi, Scott Seymour, Shawn Corbin, Arvind Krishnaswamy, Ed Drown, and especially Richard "Ricky" Schalek.

Dr. Drzal, I am honored to say that I was once a student of yours, and I hope that I lived up to what it means to be a student of L.T. Drzal. I appreciate your guidance and patience, and most of all for being a wonderful mentor, guide, and friend.

TABLE OF CONTENTS

LIST OF TABLES

1.

2.

3.

4.

5.

6.

7.

8.

9.

10.

11.

12.

13.

14.

15.

16.

17.

18.

19.

LIST OF FIGURES

20. Fig

21. Fig

22. Fig

23. Fig

24. Fig

25. Fig

26. Fig

27. Fig

28. Fig

29. Fig

30. Fig

31. Fig

32. Fig

33. Fig

34. Fig

35. Fig

36. Fig

37. Figu

38. F

39. F

40. F

41. F

42. F

43. F

44. F

45. F

46. F

47. F

48. F

49. F

50. F

51. F

52. F

53. F

54. F

55. F

56. F

INTRODUCTION

An energy absorbing material manufactured from polypropylene and polyethylene terephthalate fibers was developed. This material is installed on the A, B, C pillars along with the side rails of the headliner in order to help OEM's meet the requirements of Federal Motor Vehicle Safety Standard (FMVSS) 201 - Occupant Protection in Interior Impact by 1998. In order to be an acceptable energy absorbing material for this application, it must meet a HIC number of 1000 or below for various OEM's. The material is relatively new and performs in an acceptable manner in its current configuration but it has not been analyzed for its optimum energy absorbing potential relative to its composition and configuration. The goal of this project is to determine how this material absorbs energy, and then to maximize the energy absorbing potential in order to meet a HIC number of 1000.

In order to accomplish this, the EAM will be tested and analyzed on both macroscopic and microscopic levels. Impact testing will be performed in order to gain an understanding of how the EAM responds to damage, looking both at large scale damage and deformation, along with microscopic, fiber level, damage and deformation. Thermal analysis of the material will be performed in order to gain an understanding of the constituent materials themselves and their interactions with one another under various processing conditions. Microscopy will be necessary to evaluate and explain material behavior.

LITERATURE REVIEW

General Information

The use of composites is becoming more and more prevalent in our society today. We see composites being used in a number of industries such as recreational equipment, automotive, aircraft, and aerospace. Manufacturers are using composites more to reduce weight in their products, but also to take advantage of properties like high strength to weight and high stiffness to weight ratios, and to dissipate energy. Car bumpers and interior car component structures are examples of composites being using to provide a degree of occupant safety. Composites are being used to dissipate energy now that safety is becoming a higher priority of automakers due to the creation and modification of stringent safety standards.

Of the nearly 5800 cases of severe head injuries involving passenger cars and light-duty trucks and vans, 37% are fatalities and 67% are serious injuries with an abbreviated injury scale (AIS) rating of three or greater. These injuries involve primarily the front-seated occupants, with most of them involving the driver [2]. Impact with the upper interior components of automotive vehicles is the leading cause of head injury for non-ejected occupants killed in an automobile crash. Accident data shows that occupant head injuries result primarily from head contact with a vehicle's pillars, side rails, headers and other components during a crash [1].

Various standards created by the National Highway Traffic Safety Administration (NHTSA) and the Department of Transportation (DOT) are in effect to address this issue:

Std. No. 208 – Occupant Crash Protection, limits the forces and accelerations that are imposed on the head of a crash dummy in a frontal, 30-mph crash test. It has been effective at reducing actual fatality risks and together with the use of safety belts, has significantly reduced fatality risk.

Std. No. 201 – Occupant protection in an interior impact too effect on January 1, 1968. The standard set requirements for instrument panels (IP), interior compartment doors, seat backs, sun visors, and armrests (A/R) to lessen injuries to persons thrown against them in crashes. A large number of occupant injuries and fatalities result from head impacts with upper interior components not covered by Std. No. 201 [1].

FMVSS 201

To perform the tests of FMVSS 201, a modified headform is used. This headform lacks the nose of the Hybrid III head to eliminate interference from the nose during testing. The current headform is instrumented with tri-axial accelerometers, positioned to measure the acceleration at the headform's center of gravity. These measurements are used to calculate the magnitude of the potential for injury resulting from the impact.

The 15-mph test speed was chosen because it is the current test speed used in Std. No. 201. It is the average speed at which the onsets of serious injuries occur. It also represents the velocity at which the headform contacts the

upp

is im

is ap

adva

impa

comp

4.5 k

m/s.

relati

free m

It repr

actual

Std. No

school b

upper interior component and is lower than the actual speed at which the vehicle is impacted. NHTSA has concluded that the proposed 15-mph FMH impact test is appropriate for all components regardless of their locations.

The flight of the headform should be "free-motion" rather than guided. The advantage is that the FMH can simulate the glancing and non-perpendicular impacts experienced in real world crashes.

A new revised test procedure mandates that all upper-vehicle interior components should be tested by impacting a featureless Hybrid III headform of 4.5 kg that travels in free-flight mode for not less than 25 mm at a velocity of 6.70 m/s. The tests are to be conducted at a temperature of 22.5°C ± 3.5°C with a relative humidity between 10-70%.

HIC is calculated using the acceleration readings from an instrumented free motion headform (FMH) and transforming it to a dummy equivalent HIC(d). It represents the HIC that would normally be experienced by a full dummy or actual vehicle occupant.

$$HIC(d) = .75446(FMH\ HIC) + 166.4$$

$$FMH\ HIC = [1/(t_2 - t_1) \int a\, dt]^{1/2} (t_2 - t_1)$$

a = resultant acceleration expressed as a multiple of g

$(t_2 - t_1)$ are any two points in time during the impact which is not greater than 36 ms.

The HIC is an appropriate injury criterion to measure injuries by NHTSA. Std. No. 208 occupant crash protection, No. 213 child restraint systems, No. 222 school bus passenger seating and crash protection each uses a HIC limit of

1000. Research has shown that using an upper limit of 1000 HIC prevents serious injuries in actual crashes.

For each impact zone, the proposed test procedures defined a range of approach angles at which the FMH would strike any point in that zone. The headform could be launched from any location inside the vehicle, provided that the specified approach angles and the following restrictions were met. The headform had to travel through the air for a distance of at least 25-mm before contacting the vehicle interior surface. At the time of initial contact between the headform and the vehicle, a specified portion of the headform's forehead must contact some portion of the target circle and on a portion of the headform may contact any part of the vehicle outside of the specified impact zone.

Impacting points usually involve areas of the car structure where several sheet- metal stampings or reinforcements come together. The distance of the impact targets from these joints is usually around 125 mm. HIC(d) values depend on the location evaluated and the direction of impact or approach angles.

The acceptance criterion is now based on a functional relationship that combines the acceleration and time rather than an absolute headform acceleration value. The ideal energy dissipater is represented by a square-wave load/deflection response [1].

According to GE plastic engineers, the revised FMVSS 201 will force the redesign of the upper material trim, with pillars being the greatest challenge. GE plastic engineers also think that the HIC(d) is driven mainly by design rather than materials [2].

Energy Absorbing Materials

Various materials have been investigated in order to meet energy absorbing requirements in FMVSS standards such as steel, thermoplastics, polymer and polyurethane foams. Steel "crush-cans," are manufactured to yield plastically under load. This usually involves axial crushing against the rigid member. Crush-cans, however, are limited since they have a potential for bending rather than crushing axially when non-axial forces are encountered. Thermoplastics are a bit more flexible than steel. They, however, are also sensitive to non-axial loading like steel crush-cans. They offer greater off-axis load-bearing capability than steel crush-cans, but the load-bearing capability is reduced and may cause plastic behavior. Polymer foams can perform well in all load directions and can have a large range of crush characteristics. They are more versatile since they can be tailor made [3].

Polyurethane (PU) foam is used in various light duty trucks and multipurpose passenger vehicles (MPV) to improve vehicle crashworthiness. They have a very good history of effective energy-absorption properties. They are currently used in vehicle interiors and exteriors for applications such as knee bolsters to help OEM's meet FMVSS 208 and hip and shoulder bolsters to help meet FMVSS 214. Energy is absorbed through elastic deformation or the shattering of cell walls and struts in PU foams. PU foams can be easily altered and since it originates as a liquid, it can be foamed in place behind interior trip parts eliminating the need for fasteners and adhesives. PUs are also

advantageous since they exhibit isotropic energy-absorption behavior and are not sensitive to impact direction [3].

PU foams can absorb energy through different mechanisms. Recoverable foams store a great deal of energy through elastic deformation of semi-flexible cell walls and struts. After impact, the stored energy is released as rebound energy. Some energy is also absorbed by the deformation of the PU cells and struts. Since they are very flexible, recoverable foams can usually recover almost all of their original shape after impact and can even withstand multiple impacts. Rigid foams, however, dissipate energy through shattering of cell walls and struts. They are usually non-recoverable. They will also absorb more efficiently with less rebound than recoverable foams. They are more useful in limited space areas where impact energy must be absorbed [4].

Honeycomb structures are another method of absorbing energy. They are continually used in impacting faces to simulate actual crash conditions without damaging test fixtures. Man-made honeycomb is manufactured by fusion bonding, adhesive bonding, or welding thin sheets of paper, plastic, or metal together. Aluminum and polypropylene and polyethylene honeycomb structures are some examples. Honeycomb absorbs energy by crushing under loads. It provides efficient "g" limit protection in applications such steering columns and knee bolsters. Under compression, it carries load through the stabilized cell walls, as failure occurs, the walls locally fail along the edge. This failure continues along the cell walls until a solid block of material is achieved through the continual collapsing of the cell walls [5].

Energy absorbing thermoplastics such as general-purpose low glass acrylonitrile butadiene styrene (ABS), polycarbonate (PC), low gloss PC/ABS, and high crystalline polypropylene (HCPP) are helping to meet and exceed various FMVSS requirements. These materials are mainly used in pillar trims in the interior of a vehicle. Testing of these four materials in FMH testing by Locke and Clark showed the ways in which these materials managed energy varied significantly. This leads to the conclusion that HIC(d) is driven mainly by design than material. Pillars molded from ABS, PC/ABS, and PC crush during impact, which is the desired behavior since it provides continual energy management during impact. HCPP ribs fractured at and around the impact site. Due to this type of failure, the force of the impact is transferred to the underlying steel surface since energy absorption by the plastic pillar ceases [6].

New materials are being developed constantly to meet the continually changing and more stringent FMVSS standards. One of these materials is an energy absorbing material composed of PP and PET fibers. The material is confined in a 75/25 ratio has been fabricated for its energy absorbing potential. The material is processed at set conditions, which melt the PP but not the PET resulting in a stiff fibrous material. The material has a unique material geometry and polymer combination. This project focuses on figuring out how the material functions and ways to improve the energy absorbing potential.

MATERIALS and METHODS

Materials

A new material composed of recycled polypropylene and polyethylene terephthalate post-industrial fibers was created. The patented unique structure formed from this material is being used as an energy absorbing material in the interior of vehicles, in areas such as the A, B, and C pillars, along with the side areas along the headliner.

The process of manufacturing the EAM starts with post-industrial PP and PET fibers mixed in a 75/25 ratio, followed by processing in a special "weaving" machine, which weaves the fibers into a "vertical" fabric-like material at a density of 1200 g/m^2. The weaved material is then cut into shape and then put in a convection heater at 216°C for one minute while being compressed to a thickness of five millimeters. The hot material is then taken out of the oven and placed in the EAM mold. The material is compressed over a mold, which also stretches the material in a water-cooled mold (16°C) for approximately 30 seconds.

Polyethylene terephthalate is a high-performance thermoplastic. Its chemical structure is shown in Figure 1 below.

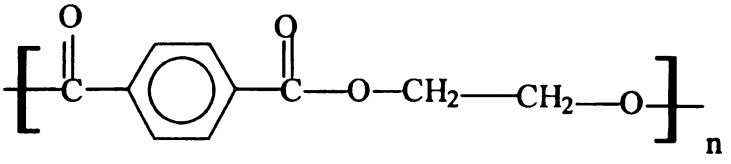

Figure 1: Chemical structure of PET [8].

In its crystalline form, the PET has a very high flex modulus and a high heat deflection temperature, but very low impact strength. Impact strength can be improved by adding elastomers or other fillers [7]. Polypropylene (PP) has good chemical resistance along with satisfactory mechanical properties. Its chemical structure is shown in Figure 2 below.

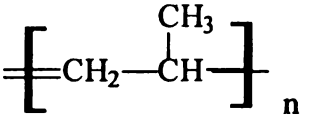

Figure 2: Chemical structure of PP [8].

It is relatively inexpensive and is easy to process. PET has good chemical and solvent resistance and better mechanical properties than PP. It is difficult to process though. Both materials are used frequently for packaging applications [7].

PP and PET are incompatible due to differences in their chemical nature and polarity. Blending them will create a clear two-phase morphology.

Generally, the strength and stiffness of their blends increases with increasing PET content, but they still exhibit very poor impact strength [7].

Studies analyzing the compatibility of the two materials by Morye et al, showed that the viscosity of a PP-PET blends was lower than that for PP even though PET has a higher viscosity. This seemed to indicate incompatibility between PP and PET. In addition, adding PET to PP resulted in a lower tensile strength of PP showing again that the two are incompatible [7].

Studies by Cheung and Chan showed that increasing the weight percentage of PET to PP increased the modulus. "Good interfacial bonding is required if the blend is to have good mechanical properties. The mixing of PP and PET results in clumps of one phase dispersed in the other" [9]. Due to the incompatibility between the two polymers, the interfacial adhesion is very poor. Thermodynamics does not favor the mixing of the two polymers. "The interpenetration of chains from the two polymers at the interface is poor" [9]. This poor interpenetration leads to poor interfacial adhesion.

An energy absorbing material consisting of PP and PET fibers confined in a 75/25 ratio has been fabricated for its energy absorbing potential. The fibers are processed at certain conditions, which melt the PP but not the PET resulting in a stiff fibrous material. The unique material geometry and polymer combination provides energy absorption capacity in the structure.

Material and Processing

The first set of samples was fabricated using the parameters shown in Table 1. Mat material at three different densities were evaluated at five different

densities were evaluated at five different temperature conditions to see what effect the amount of material and the temperature had on the EAM. Mat material consisting of 70% recycled PP and 30% recycled PET was first cut into various sections from three different density material rolls. After the mat material was gathered, the material was heated to the desired temperature for two minutes in a convection oven. While the sample is being heated the oven, the sample is compressed to a five-mm thickness. The heated and compressed mat material is then placed in the corrugated mold, which is completely automated with a pre-programmed open and close cycle time.

During the fabrication of these samples, large amounts of shrinkage of the material were seen when the material was removed from the heater to the mold at both the 193°C and 204°C temperatures. As a result, the samples fabricated at these two temperatures were thicker than the rest of the samples fabricated at 216°, 227°, and 238°C.

	193°C	204°C	216°C	227°C	238°C
1000 g/m²	1	2	3	4	5
1200 g/m²	6	7	8	9	10
1400 g/m²	11	12	13	14	15

Table 1: Density vs. Temperature parameters used for first group of samples.

The second set of samples was fabricated at Michigan State University (MSU) to evaluate stiffness as a function of thickness within the material. Sample

sheets of various thicknesses had to be fabricated. The thicknesses were 1.5, 1.2, and .65-mm. These measurements corresponded to different thickness regions (A, B, C, D) of the EAM structure determine from previous micrographs where regions A and C were approximately 1.5-mm thick, region B approximately 1.2-mm thick, and the apex region D was approximately .65-mm thick. Flat samples were processed in a four platen Carver Laboratory Press dual daylight Model 2731 hydraulic press (Figure 3). The first set of platens were heated to 216°C, the second set of platens were set at approximately 16°C. Samples were made with virgin PP and PET at a 75/25 PP and PET mixture ratio. Unconsolidated mat samples were placed between Teflon coated glass fabric release film and then compressed to approximately five-mm using steel shims at a maximum pressure of 24 KSI on the press. After heating, the hot mats were then compressed between two steel plates to the various thicknesses that were desired. While this was being done, the platens were cooled with running water to approximately 16°C for approximately three minutes until the bottom platen reached 66°C. After three minutes, the compressed material and steel plates at various thicknesses were then inserted in the upper platen for two minutes with the appropriate shims and then removed. The fabricated sheet samples were then removed from the steel plates and then measured using a micrometer along the edges of the sheets to verify the thickness of the samples.

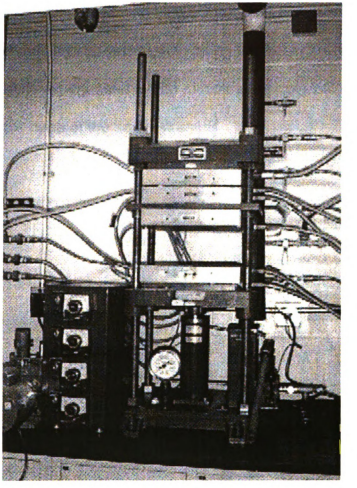

Figure 3: Carver laboratory press Model 2731.

In addition, a third set of samples was fabricated using the processing conditions shown in Table 2 to evaluate the effects of different processing conditions on the material. Time of the mat material in both the convection heating oven and the time in the mold, the temperature of the heater, and displacement of the mold were of concern. Samples were fabricated on a large, scaled up mold and were processed (Figure 4) in order to get sample sections

large enough for testing. Samples needed to be representative of production run samples since the samples fabricated at MSU were not representative. Each region experiences different stresses when being formed in the mold, but due to the lack of constraints experienced by the samples fabricated at MSU, these samples experience none of the same stresses.

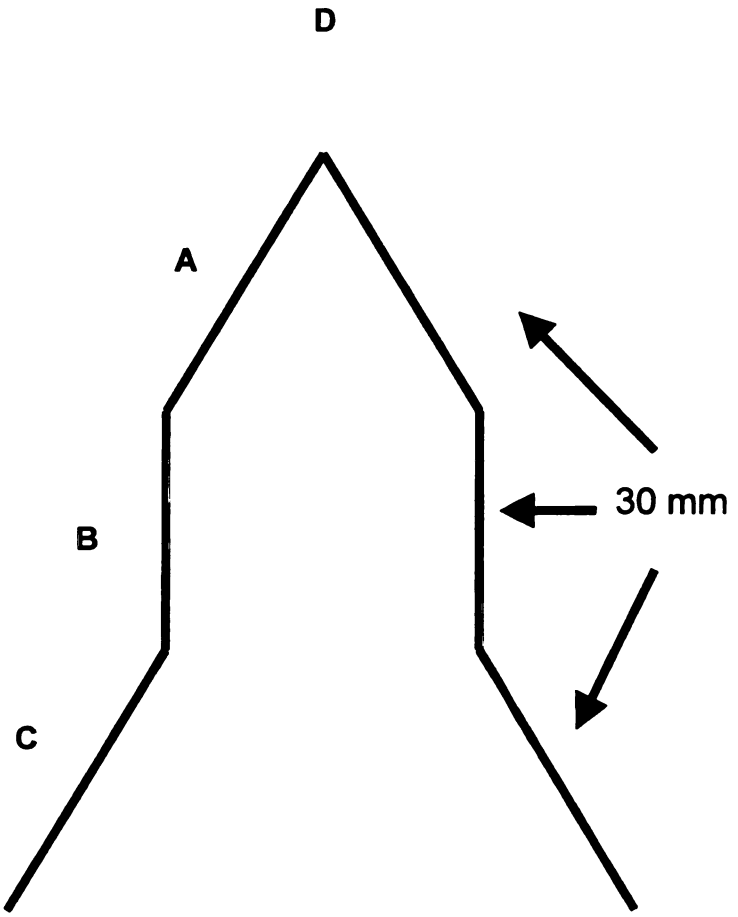

Figure 4: Drawing of enlarged EAM mold.

Samples were first heated in a convection oven and formed in the enlarged mold for the temperatures and times shown in Table 2. Samples were approximately three times the original size of the EAM element.

	TIME 1 (HEATER sec)	TIME 2 (MOLD sec)	TEMP (°C)	PRESSURE (DISP mm)
TIME 1 (HEATER sec)	60 90 120	60	60	60
TIME 2 (MOLD sec)	45	30 60	45	45
TEMP (°C)	216	216	216 227 238	216
PRESSURE (DISP mm)	1.5	1.5	1.5	1.5 1.25

Table 2: Matrix of Time, Temperature, and Pressure Processing Conditions.

In order to evaluate this EAM and its properties, a variety of different testing and characterization instruments were used, including differential scanning calorimetry, optical microscopy, Dyna-tup impact testing, dynamic mechanical analysis, high strain tensile testing, and impact/penetration testing. The following sections discuss the instruments and methods in detail.

Methods

Differential Scanning Calorimetry

Differential Scanning Calorimetry (DSC) is a device used to determine temperature and heat flow for a given material as a function of time and temperature. It can also determine information such as glass transition temperature, crystallization, melting transitions, and heat capacity of a material.

The principal of operation of DSC involves monitoring the difference in temperature between a reference and sample while both are being subjected to a specified temperature profile. The energy difference between the two is recorded as a function of temperature. The thermal events, endothermic (heat absorption) and exothermic (heat evolution) reactions, appear as deviations from the baseline given by the DSC. Exothermic responses are positive which corresponds to the evolution of heat in the sample compared to the reference, while endothermic responses are negative which is indicative of absorption of heat. These responses can be caused by melting, oxidation, and possible phase changes occurring in the material. It is this information that helps one identify the changes which a sample material undergoes with temperature as well as identify both the material and its processing constraints.

The glass transition temperature (T_g) is characterized by the onset of motion in short segments of the polymer chain. This temperature is indicative of the amorphous regions of the polymer. Below the Tg, the polymer is hard and behaves like a glass. Above the Tg, the polymer becomes more flexible and rubbery.

The melting temperature (T_m) is the temperature at which the material goes from a solid phase to a liquid phase.

Both of these parameters are important and can be used to characterize and verify the constituent materials of the EAM and its properties.

For this project, a TA Instrument DSC 2920 was used to identify glass transition and melting temperatures of PP and PET. By obtaining these two characteristic temperatures, verification of the composition of the two polymers was achieved. The scans could also provide information about constituent purity.

Optical Microscopy

Optical microscopy is useful for evaluating a specimen at the microscopic level using instruments such as optical microscopes or scanning electron microscopes (SEM). For this research both an Olympus BH2-UMP optical microscope with a barrier and band pass filter and an environmental scanning electron microscope (ESEM) were used to examine specimens.

Samples were mounted in Buehler sampl-kwick fast cure acrylic resin and polished on an Abramin sander with 240 to 4000 grit paper for three and a half minutes with approximately 50 N of force. Optical micrographs were recorded using an Olympus BH2 optical microscope. A typical mounted sample containing a cross-section of the EAM is shown in Figure 5.

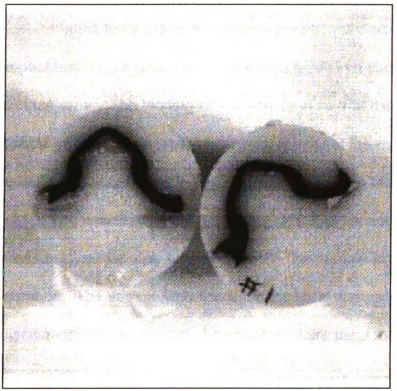

Figure 5: Mounted sample specimen of the EAM.

Samples were also impregnated with Struers Epofix epoxy resin containing a fluorescent dye by applying a vacuum to the sample at room temperature for 10 minutes. Impregnated samples were then cured overnight and then mounted in Buehler sampl-kwick fast cure acrylic and polished on an Abramin sander with 240 to 4000 grit paper for 3.5 minutes and approximately 50 N of force as before. They were then examined using an Olympus BH2-UMP optical microscope with a barrier and band pass filter. These samples were also examined with an ElectroScan environmental scanning electron microscope (ESEM).

Dyna-tup Impact Testing

Impact testing is quite different from compression or tensile testing. In impact testing, samples experience high loads in a shorter time over a small surface area. The loading rate is very high so that there is no relaxation and heat is generated. A totally different behavior of the material can be detected under impact conditions than under slow strain rate testing.

The velocity and force are very critical in impact testing. The velocity is measured immediately before contact. The sample is rigidly fixed to eliminate vibration. The sample vibration after impact is dissipated energy. Heat is also dissipated after the impact. Strain gauges are used to measure the deformation experienced by the sample. A piezoelectric force transducer records the force which is converted to a load and then to a stress. A force versus time or force versus displacement graph can be generated from the impact data. The following step by step process is used to calculate the energy.

The force is measured by knowing the acceleration, which is F(t)/m, where F(t) is the force as a function of time, and m is the mass. This is the acceleration at the contact point. By integrating the acceleration [$\int a(t) = \int dv/dt$], one can find the velocity. Since the initial conditions are known, the velocity history is known at any instant of time. By integrating the velocity [$\int v(t) = \int dx/dt$], one can obtain the displacement. Plotting the force [F(t)] versus the displacement [x(t)] yields the energy curve. Energy is equal to the force multiplied by the distance.

There are some factors to consider when doing Dyna-tup testing. One is the assumption that the motion of the tup (impactor) impact is equal to the movement of the specimen, assuming rigid bodies. The linear variable displacement transducer (LVDT) only measures the displacement of the backside of the specimen, so any deformation occurring in the other direction is ignored. The energy from the tup is not necessarily equal to the energy absorbed by the material. The exact velocity of the tup at the impact point must be calculated.

Since it is known that the force on the specimen (the EAM sample) equals zero right before impact and after the tup rebounds off the material, the period between these two events is the force vs. time history. The following step by process is used to calculate the impact velocity [11].

VELOCITY OF A FREE FALLING BODY

$V_1 = V_o + g(t_1 - t_o)$ (initial velocity before impact)

$V_2 = V_o + g(t_2 - t_o)$ (final velocity after impact)

Equate V_o yields:

$V_2 = V_1 + g(t_2 - t_1)$ (second velocity in terms of first velocity) (1)

POSITION OF A FREE FALLING BODY

$x_1 = x_0 + V_o(t_1 - t_o) + g/2\ (t_1 - t_o)^2$ (first position)

$x_2 = x_0 + V_o(t_2 - t_o) + g/2\ (t_2 - t_o)^2$ (second position)

Equate x_o yields:

$V_o = (x_2 - x_1) + g/2\ [(t_1 - t_o)^2 - (t_2 - t_o)^2]/\ t_2 - t_1$

Let t_o, x_o, $V_o = t_1$, x_1, V_1 yielding:

$V_1 = (x_2 - x_1)/(t_2 - t_1) - g/2(t_2 - t_1)$ (initial velocity in terms of displacement and time) (2)

Substitute eq'n (2) into (1) yields:

$V_2 = (x_2 - x_1)/(t_2 - t_1) + g/2(t_2 - t_1)$

The Dyna-tup machine itself has a maximum drop height of approximately five feet. Subtracting out the height of the impactor yields a total height of approximately three feet. This translates to an impact velocity of approximately 15.2 km./hr.

Preliminary tests using a Dyna-tup machine were conducted using a new tup fixture, which was designed and fabricated especially for the testing, shown in Figure 6.

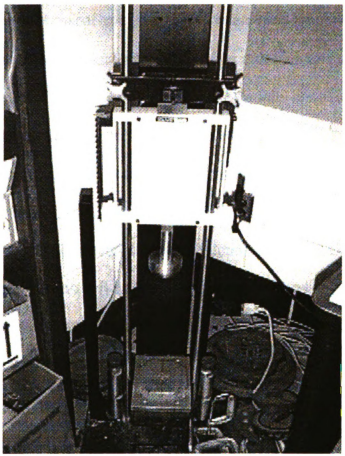

Figure 6: Dyna-tup testing set-up.

The original set up was modified in order to accommodate the EAM and its requirements for testing. The most crucial part of the set up was aligning the tup and the bottom plate. It was crucial that the tup was directly over the point of impact so that the transducer, which is located underneath the aluminum plate, would not be damaged. The load cell could only handle a maximum load of approximately 909 kg without damage.

Dynamic Mechanical Analyzer

A dynamic mechanical analyzer (DMA) is an instrument, which is designed to measure visco-elastic properties, like modulus and energy dissipation for both soft and stiff solid materials. Various shapes and sizes along with various clamping arrangements can be used.

A DMA works by applying an oscillatory or sinusoidal strain or stress to a material and then measuring the resulting stress or strain developed in the material. Mechanical deformation is applied to samples by the DMA drive motor sinusoidally. Deformations can be applied in a step fashion or at a fixed rate. For an ideal solid obeying Hooke's Law, the resulting stress will be proportional to the amplitude of the applied strain. The phase angle between the stress and strain will be 0°. For an ideal fluid obeying Newton's Law, the resulting stress will be proportional to the rate of strain. The phase angle of the stress will lead the phase angle of the strain by 90°. For visco-elastic materials, a complex modulus is introduced, E^*. This consists of a storage modulus E' and a loss modulus E'', thus giving $E^* = E' + E''$. The storage modulus is a measure of stiffness, where the loss modulus is a measure of the amount of energy retained after testing [12-13].

For this project, both a TA Instruments 2980 and Du Pont 983 DMA were used.

The TA Instruments 2980 DMA operates by choosing a particular set-up and then programming the respective conditions. For this project, the three-point bending clamping mechanism was installed and calibrated (Figure 7). Samples were tested in a horizontal set-up. The set-up involved using the liquid nitrogen-cooling accessory, along with compressed air. Samples were run using a multifrequency mode, which tests the sample at a constant amplitude, and at a constant frequency. The autostrain was also used. The autostrain puts a static force on the sample and adjusts this value during the experiment [14].

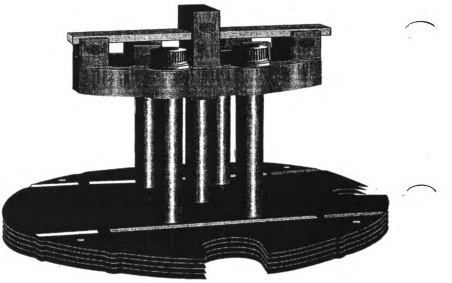

Figure 7: TA Instruments three-point bending set-up [12].

The Du Pont 983 DMA operates under four modes of operation. For this project, the fixed frequency oscillation mode was used. Samples were tested in

a vertical clamping set-up. Samples were clamped between two parallel arms, which are mounted on low-force flex pivots which only allow motion in the horizontal plane. The distance between the arms can be adjusted. An electromagnetic motor attached to one of the arms drives the sample to the desired amplitude. A linear variable differential transformer (LVDT) mounted on the driven arm measures the sample response to the applied stress. An adjustable thermocouple is mounted close to the sample to give accurate feedback information to the temperature controller.

The DMA was used in this project to determine how the EAM was affected by processing parameters. Obtaining these profiles of a material is a very accurate way of predicting how a material will respond to certain conditions. By plotting the E' as a function of temperature, the stiffness profile of a sample can be seen as the temperature goes from low to high temperatures or vice versa. The DMA was also used to see at what point a material will degrade when subjected to various strain rates. This was done by subjecting samples at room temperature to consecutive strain sweeps. (A strain sweep test is when the sample is subjected to various levels of strain repeatedly.) The storage modulus was then plotted versus various percent strain. When repeated several times, the point at which the storage modulus decreases at a particular strain indicates the point of material degradation. The DMA data also revealed the true material machine direction of the material. This was done by testing a sample in machine direction and cross-machine direction. The resulting storage moduli were plotted

against temperature. The difference in moduli was indicative of anisotropy between machine and cross-machine direction.

High Strain Tensile Machine

In order to determine the ability of the material to absorb energy under impact conditions, high strain tensile tests were performed using a hydraulic tensile testing machine. The tests at various strain speeds, given in meters per second (mps), were performed at the IKV at RWTH – Aachen University using the machine and instrument set-up shown in Figure 8. The auxiliary equipment used in the experiments included a water cooling system, a ww700 transient recorder, a Kistler 5001 charge amplifier, and Zwick REL control system.

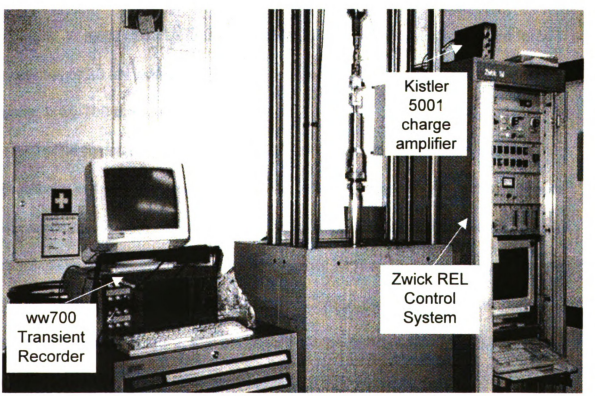

Figure 8: High Strain Tensile Set-Up.

The high strain tensile testing system operates in the following manner. The control system must be on and warmed up for a period of time. The system parameters for warming up the machine are as follows: the machine is first reset, the pump is turned on, a sinusoidal wave function is selected, and the negative test direction is chosen. The Level and Amplitude control the height of the lower testing arm and grip. The Level is raised to approximately 400 and Amplitude is raised to approximately 180. The system should run for approximately 10 minutes before changing the parameters for testing.

For testing specimens, the following parameters were used: a ramping wave function, and a single and positive (tensile) testing direction. The "active" button was also set, which activates the machine to be able to test at the higher speeds. A Kistler 9331A force gauge was used, which had a maximum force potential of 20 kN was used for these experiments. The data was recorded using a ww700 transient recorder.

The hydraulic tensile machine differs from a normal tensile machine in that there is a pre-displacement distance, which is set on the lower grip (Figure 9) before the system is activated. This pre-displacement distance enables the machine to accelerate to the constant velocity chosen for testing. For example, if you want to test the sample at a strain of 6.7 mps, the system cannot automatically attain the ample speed of 6.7 mps without allowing an initial displacement to achieve this velocity.

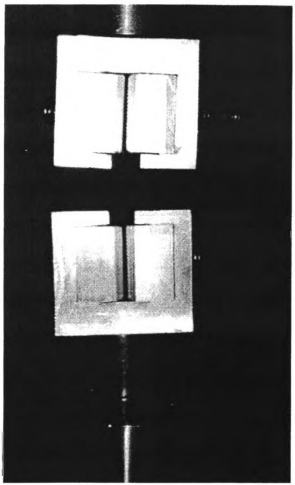

Figure 9: High strain tensile specimen.

The samples were cut out using a steel dog-bone stamp and hand press. The dog-bone specimens were eight cm long and 1.5 cm wide, and had a gauge length of 3.0 cm. Samples were tested at approximately 6.7, 4.1, and 1.4 mps. Five samples each of the B regions of all eight processing groups were tested. Since the material was very inhomogeneous it was very important to test the samples in a way that was completely consistent, measuring only the material

behavior and reducing the interference from other effects. Figure 10 shows a sample plot of the high strain tensile data.

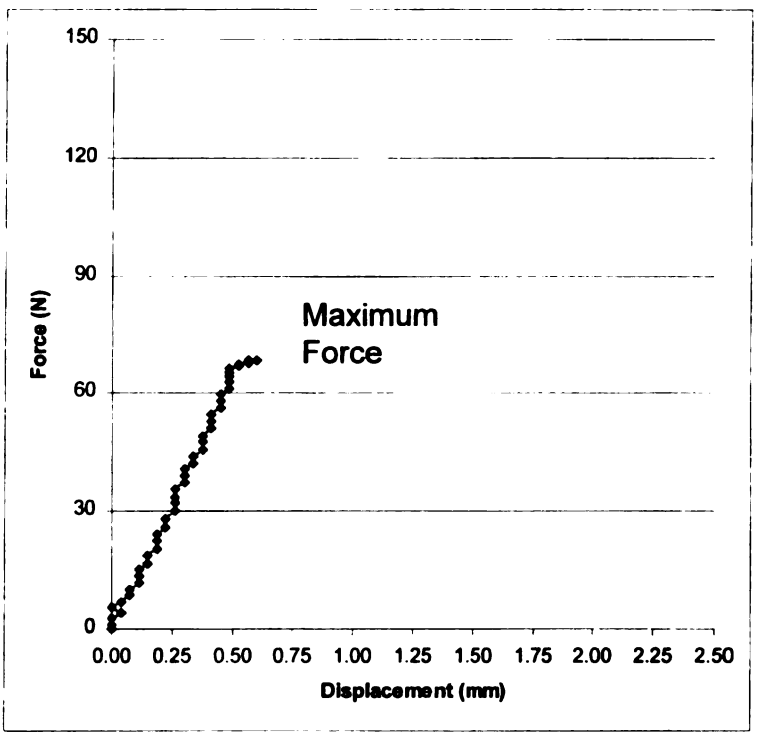

Figure 10: Sample high strain tensile curve.

Using the time-temperature superposition principle, testing samples at very high strains is representative to testing samples at very cold temperatures. Testing samples at lower strains is representative of testing at very hot temperatures. This is an important principal because this data can indicate representative material behavior at different temperatures and speeds.

Impact/Penetration Machine

In order to determine the ability of the material to absorb energy under impact conditions, impact-penetration tests were performed using the same

hydraulic testing machine used for the high strain tensile tests. The tests were performed at various speeds, given in meters per second (mps) at the IKV at RWTH – Aachen University using the machine and instrument set-up shown in Figure 16. The auxiliary equipment used in the experiments included a water cooling system, a ww700 transient recorder, a Kistler 5001 charge amplifier, and Zwick REL control system.

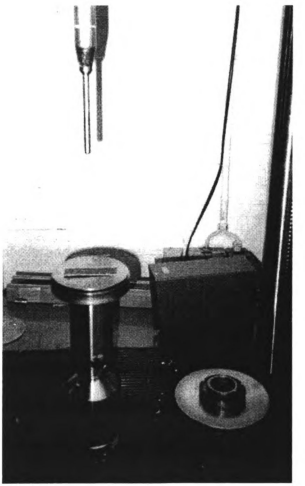

Figure 11: Impact/Penetration Set-up.

The impact-penetration machine operates in the same manner described for the high strain tests. The only difference were the set-up shown in Figure 16, which instead of tensile grips included an impact mandrel and sample platform. The impact mandrel was one cm in diameter and 10 cm long. The sample platform had a diameter of 12.4 cm. The testing parameters also varied slightly using the following parameters: a ramping wave function, and a negative (compression) testing direction. The "active" button was also set, which activates the machine to be able to test at the higher speeds. A Kistler 9331A force gauge was used, which had a maximum force potential of 20 kN was used for these experiments. The data was recorded using a ww700 transient recorder.

Similar to the high strain tensile tests, the impact-penetration tests also had a pre-displacement distance, which was set on the lower sample platform (Figure 12) before the system was activated. This pre-displacement distance enabled the machine to accelerate to the constant velocity chosen for testing.

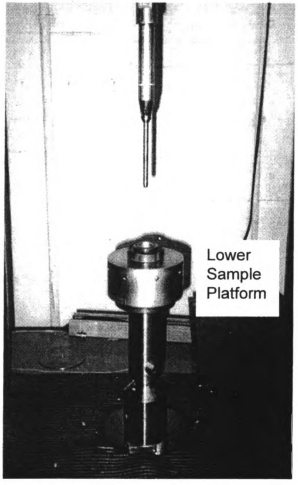

Figure 12: Impact/penetration sample set-up.

The B regions were used for testing samples. They were trimmed to a dimension of 10 cm by two cm in order to fit into the sample platform. Samples were tested at approximately 6.7, 4.1, and 1.3 mps. Five samples each of the B regions of all eight processing groups were tested. Figure 13 shows a sample impact/penetration curve.

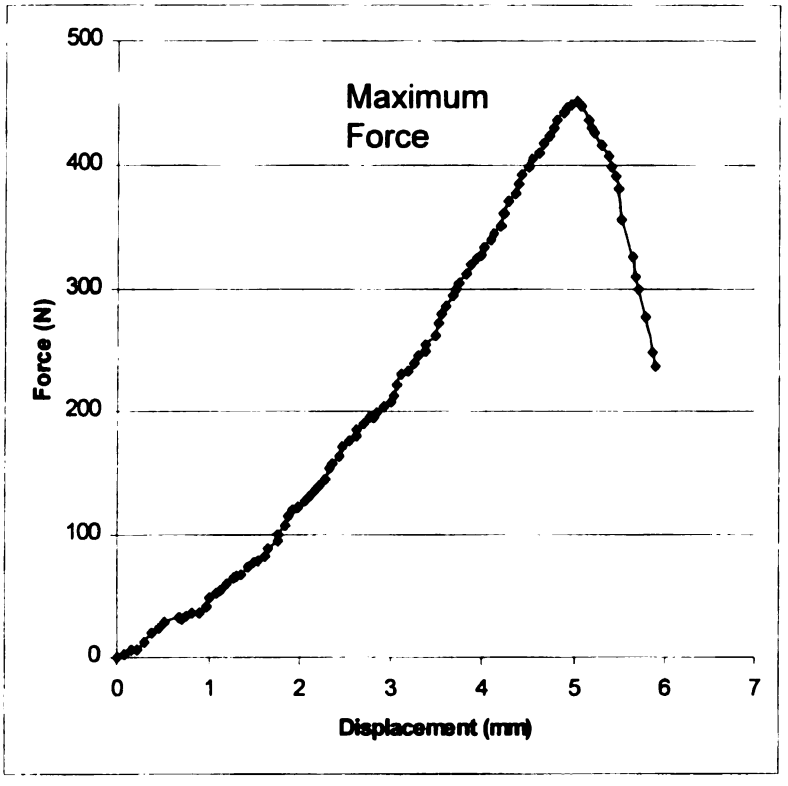

Figure 13: Sample Impact/penetration curve.

RESULTS and DISCUSSION

Thermal analysis of PP and PET EAM Fiber

DSC scans of the recycled EAM showed T_m of PP and PET to be around 167°C and 254°C respectively. These values correlated with T_m values obtained from the literature shown in Table 3.

	Tg	Tm
PP	-10 -18°C	176°C
PET	69°C	265°C

Table 3. Glass transition and melt temperatures of PP and PET [16].

Scans of PP fibers showed two melt temperatures of 167°C and 250°C respectively. The cause of the minor second melt temperature shown in the recycled PP scan is unknown and was not investigated further since the constituent materials changed from one brand of recycled material to another brand of recycled material. Scans of PET fibers showed a melt temperature of 254°C. All of the scans showed that the melt temperatures were consistent with the individual materials and the finished product.

DSC results showed that the post-industrial individual PP and PET fibers had melt temperatures around 163°C and 252°C respectively. The exothermic peaks shown in the cooling curve of the graphs are indicative of crystallite formation. Since both PP and PET are semi-crystalline materials both samples will have some indication of crystallization.

In these scans, the sample T_m is shown to decrease slightly after being tested a second time. This lowering of the T_m is possibly due to stress relaxation of the PP and PET material. The DSC did not show the T_g for the PP material, which is supposed to be visible around -20°C. Since the test was performed from –30° to 300°C, this suggests that the T_g may be present in a range lower than the range that was tested.

Optical Microscopy of the Failure Modes of EAM

To determine what type of failure each EAM element was doing while it was impacted, impacted specimens were examined microscopically. It was speculated that there was collapse in region A, buckling of the wall in region B, and crushing in areas C and D (Figure 14).

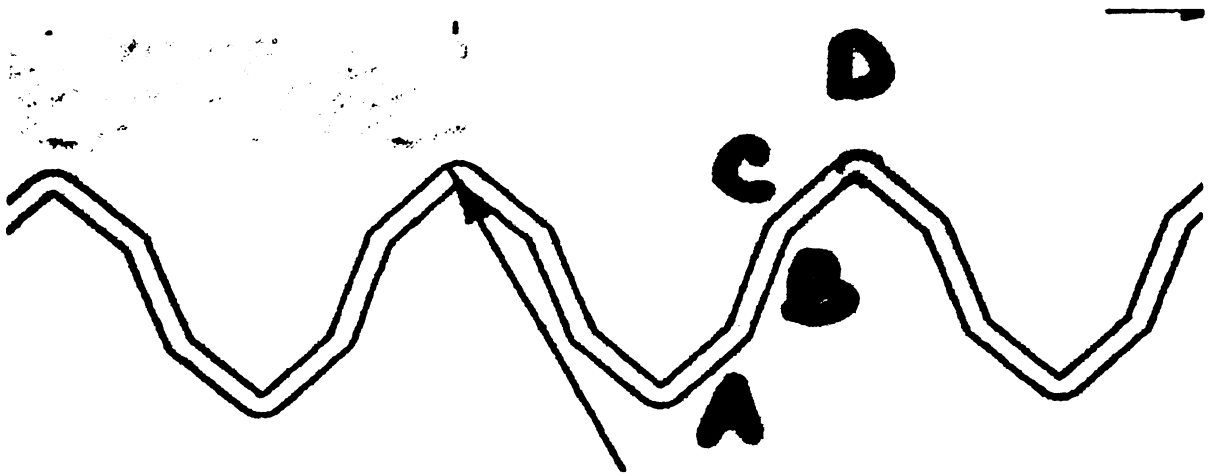

Figure 14: EAM element examined by regions.

Characterization of what the different regions of the element was very vital to understand how the material performed at both a microscopic and macroscopic level.

Failure modes of the EAM element could not be determined by optical microscopy alone. When recycled material EAM elements that were impacted were examined under a microscope, "dice" looking objects were found scattered throughout the material. It was speculated that they were cross-sectioned multi-lobed fiber bundles. This was consistently seen throughout EAM samples that were impacted or non-impacted.

In order to determine failure modes of the EAM element, non-impacted elements had to be examined in order to see what the nominal amount of damage was in an EAM element. Samples that were not impacted were impregnated with fluorescent epoxy and mounted in the methods previously described, and then examined under an Olympus BH2-UMP microscope. Non-impacted samples showed little or no fluorescent epoxy anywhere within the element shown in Figure 24. Impacted samples impregnated and mounted in the same way, however, showed that penetration of the fluorescent epoxy in high concentrated areas correlated to damage areas within the EAM element shown in Figure 25. By looking at the walls of the element, large concentrations of fluorescent epoxy can be seen, leading to the conclusion that most of the force is being absorbed by the walls of the element. By looking at micrographs, it was evident that the tip of the EAM element remained intact with almost no fluorescent epoxy showing, while the sides of the element displayed more break-up during impact. Failure modes of the various EAM sections could not determined at this time.

In addition to determining the order of failure within the EAM element, consistency of the failure observations had to be verified. Each impacted and non-impacted sample was cut in half and then examined to verify that the same failure process occurred throughout the sample. The results were consistent through the thickness with slight variations in the amount of breakup in the walls of the element.

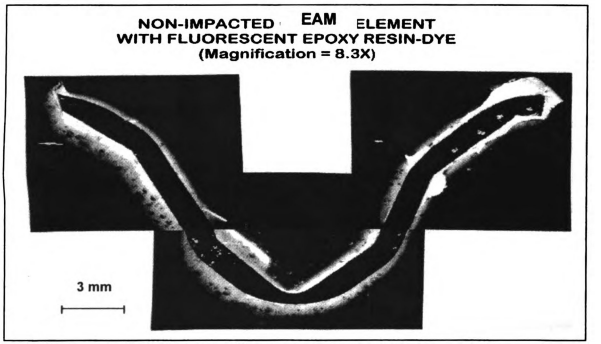

Figure 15: Non-impacted sample with little or no fluorescent epoxy in the EAM element.

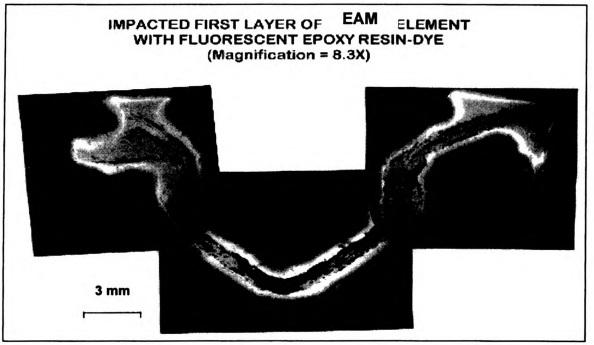

Figure 16: Impacted EAM samples with damaged areas showing high concentrations of fluorescent epoxy.

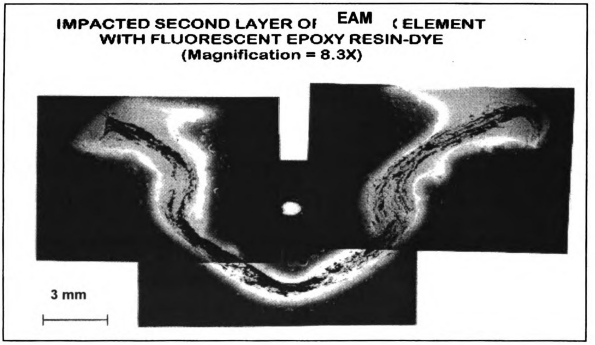

Figure 17: Second layer of EAM element showing consistent results from layer to layer.

Processing and EAM

In order to determine how processing parameters affected the energy absorbing properties of the EAM, samples were made at different processing temperatures and densities. Unconsolidated mat samples having densities of 1000, 1200, and 1400 g/m² were fabricated into consolidated panels at processing temperatures of 193 -238°C in increments of 11°C. Density was used as a variable instead of pressure since the press displacement was controlled to a 1.5-mm gap. The temperature range used to evaluate EAM properties was between the melting temperatures of PP and PET (T_m of PP = 162°C, PET = 254°C). A total of 210 tensile tests were performed at 23°C and 50% relative humidity. Tensile tests were done to measure material properties as functions of modulus and adhesion between PP and PET. Samples were tested in both the machine and cross-machine directions. Each testing group consisted of seven samples (Table 4) with tests performed with an Instron 4481 testing machine, with a 2727 kg load cell. Samples were tested using ASTM Standard D638, using a nominal strain rate of 50 mm/mm.

Modulus and total energy values extracted from the Instron tensile test data were plotted vs. temperature for both machine and cross-machine directions. Figures 18 and 19 show the Instron tensile data young's modulus and total energy values of 1000, 1200, and 1400 g/m² density samples versus temperature for machine directions respectively. Figures 20 and 21 show the Instron tensile data young's modulus and total energy values of 1000, 1200, and

1400 g/m² density samples versus temperature for cross-machine directions respectively.

	193°C	204°C	216° C	227° C	238°C
1000 g/m²	1	2	3	4	5
1200 g/m²	6	7	8	9	10
1400 g/m²	11	12	13	14	15
	193°C	204°C	216°C	227°C	238°C
1200 g/m²	16	17	18		
	A = 30 sec.	A = 30 sec.	A = 30 sec.		
	B = 45 sec.	B = 45 sec.	B = 45 sec.		
	C = 60 sec.	C = 60 sec.	C = 60 sec.		

Table 4: Matrix of Density vs. Temperature tests and 1200 g/m² density vs. time tests.

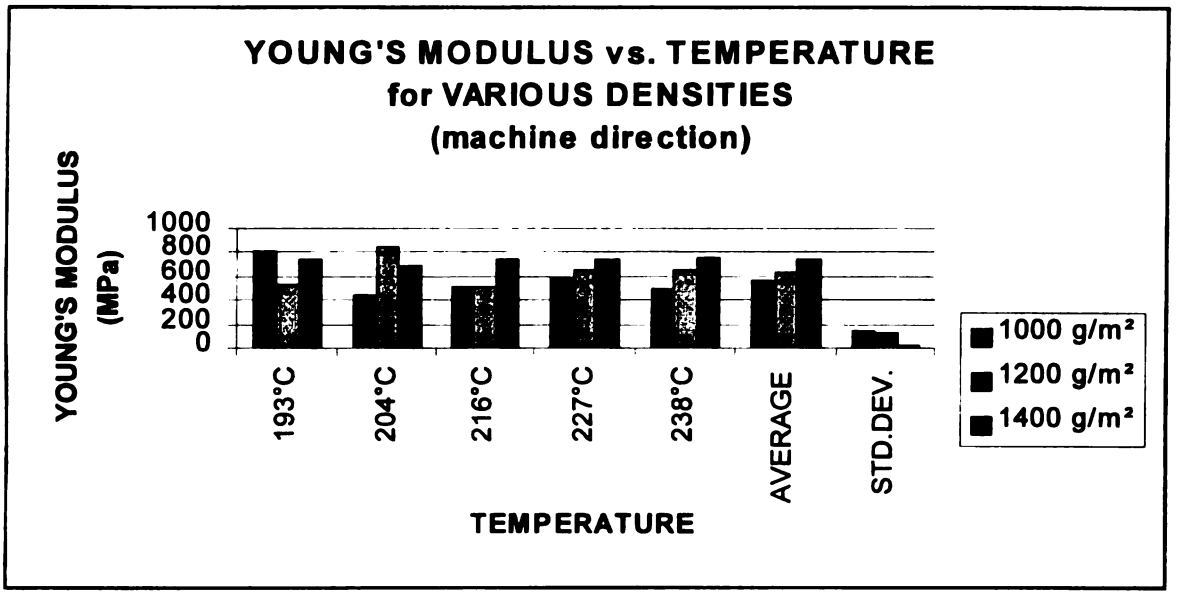

Figure 18: Instron Data Young's Modulus Values of 1000, 1200, and 1400 g/m² Density samples vs. Temperature for machine direction.

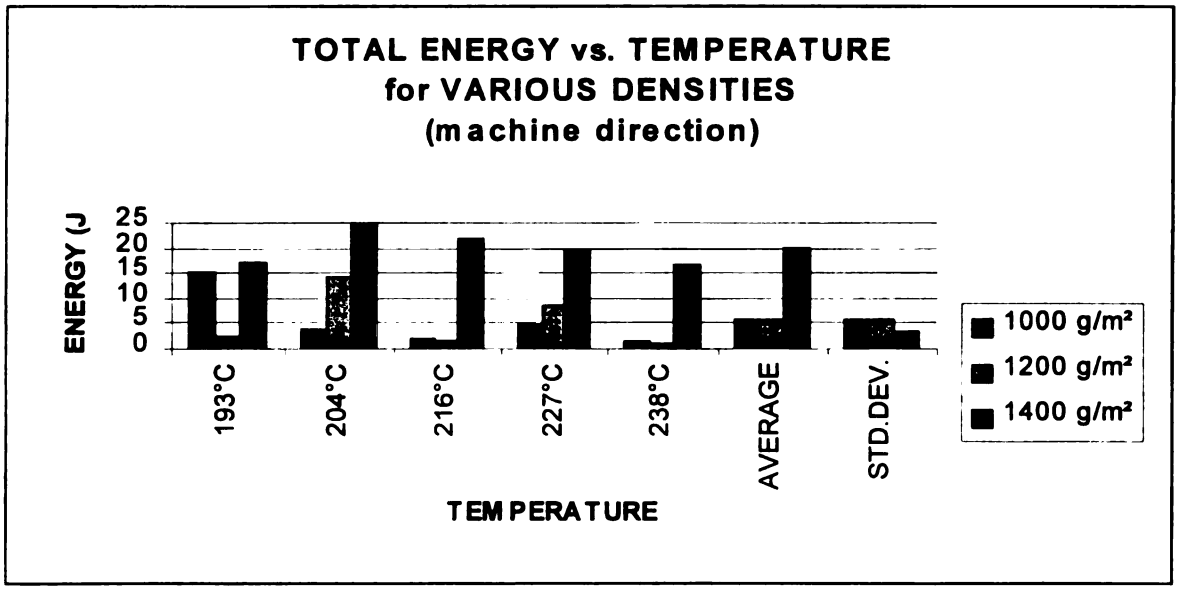

Figure 19 Instron Data of Total Energy Values of 1000, 1200, and 1400 g/m² Density Samples vs. Temperature for machine direction.

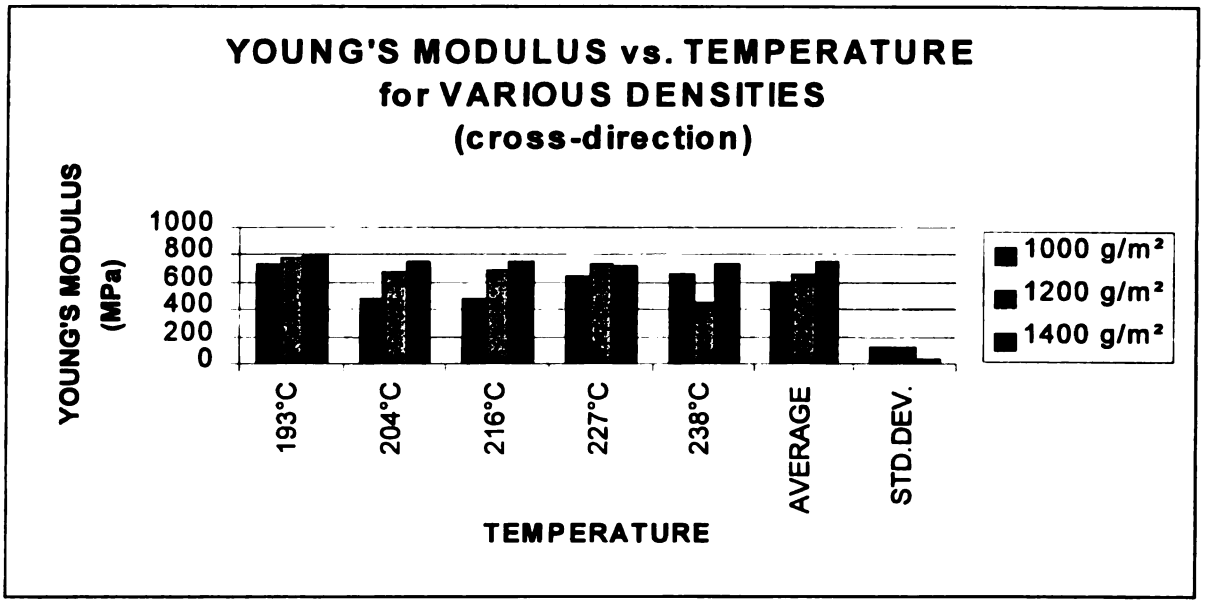

Figure 20: Instron Data of Young's Modulus Values of 1000, 1200, and 1400 g/m² Density Samples vs. Temperature for cross-machine direction.

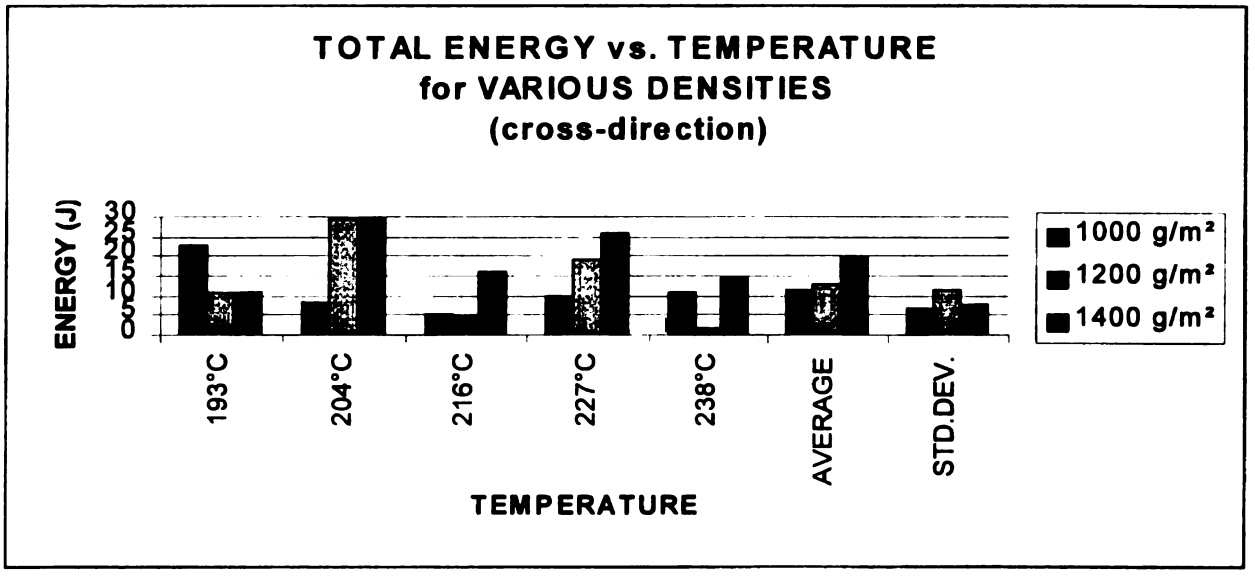

Figure 21: Instron Data of Total Energy values of 1000, 1200, and 1400 g/m² Density samples vs. Temperature for cross-machine direction.

To try and gain an understanding of the information the results were giving, a pseudo energy was calculated using the formula $W = \sigma_y^2/2E$ in order to and normalize the data. This calculation was done by making the assumption that plastic deformation after yield is a function of the sample preparation, defects, etc . The sample behavior prior to the yield point, i.e. the work of deformation area under the curve, would provide a method to normalize the data and show a dependence on the morphology of the part and not the quality of the part itself. Looking at these pseudo energies improved the scatter, but no correlation could be identified in Figures 23 and 24.

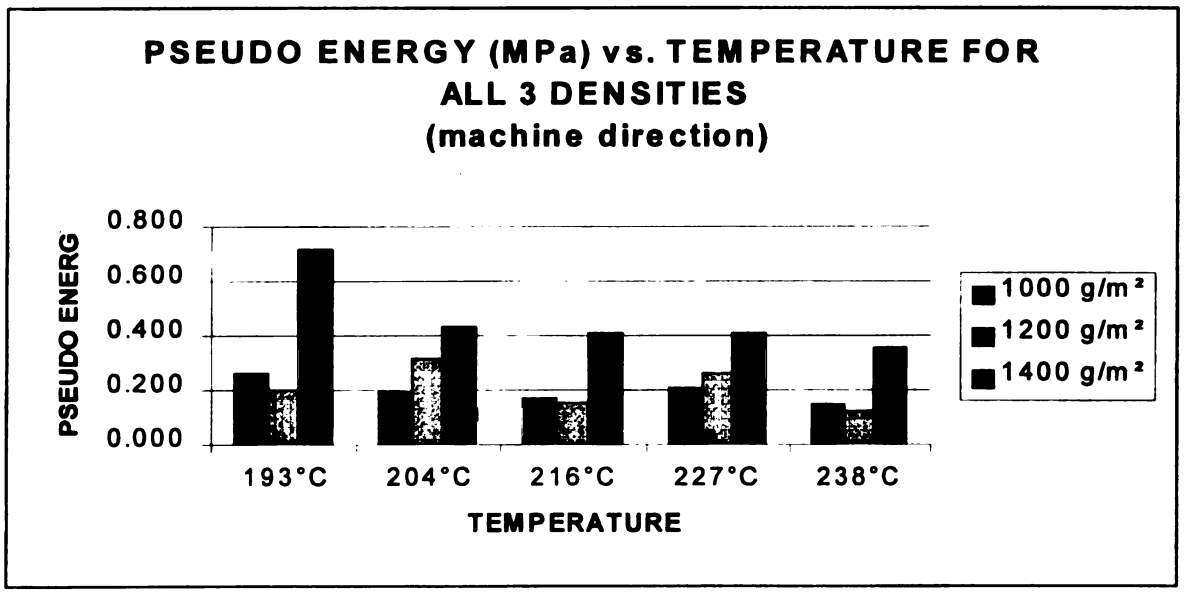

Figure 23: Pseudo-Energy Values of 1000, 1200, and 1400 g/m² Density Samples vs. Temperature for machine direction.

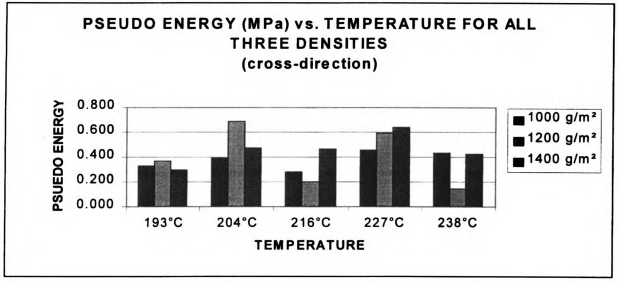

Figure 23: Pseudo-Energy Values of 1000, 1200, and 1400 g/m² Density Samples vs. Temperature for cross-machine direction.

Since little information was gained from examining the pseudo energies, there was a possibility that there was a material or process uncontrolled variable. The weights of each of the samples were measured and then examined for uniformity. Average weight vs. temperature plots for both machine and cross-machine directions were made for all three densities shown in Figures 24-26.

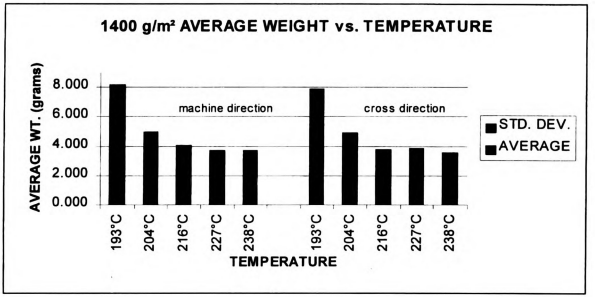

Figure 24: 1400 g/m² Density Average Weight vs. Temperature plot.

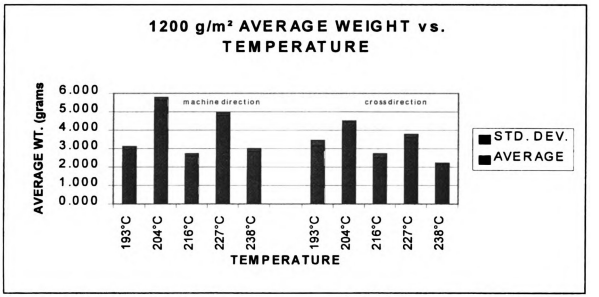

Figure 25: 1200 g/m² Density Average Weight vs. Temperature plot.

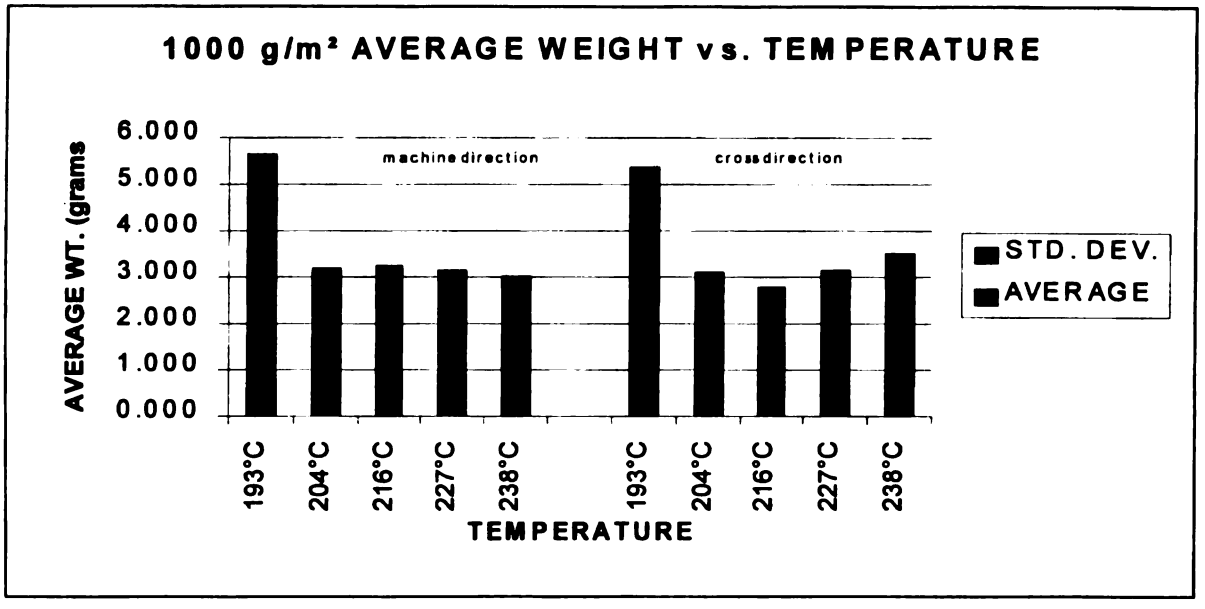

Figure 26: 1000 g/m² Density Average Weight vs. Temperature plot.

It should be noted here that samples fabricated at 193°C and 204°C showed large amounts of shrinkage. As the samples were heated to these temperatures and then removed from the heater, considerable shrinkage of the material occurred, thus increasing the density of the samples. Samples that were supposed to be at approximately 1.5-mm thick ended up being as thick as 3.8 mm. Samples fabricated at 216°C and higher showed little or no shrinkage and maintained sample thicknesses around 1.5-mm. Thicker sample weighed more.

From looking at these graphs, parallel results were seen for both the 1000 and 1400 g/m² samples. However, the 1200 g/m² results had a large amount of scatter. The 1200 g/m² samples made at 193°, 216°, and 238°C were made by

two different operators, and led to the conclusion that properties of samples are operator dependent.

After examining these results of the 1200 g/m² samples, another set of experiments using only the 1200 g/m² density mat was done. This time the sample weights were measured at temperatures, 193° - 216°C in increments of 11°C, for different periods of time in the tool, 30-60 seconds in increments of 15 seconds. Average weight of samples fabricated at 193°, 204°, and 216°C vs. time and pseudo energies of samples fabricated at 193°, 204°, and 216°C vs. time were plotted as Figures 27 and 28. The average weight vs. time plots shows that samples fabricated at 193°C showed the most amount of scatter with time in the mold. The average weight of the samples also increased as the time in the mold is also increased. Samples made at 204°C and 216°C were more consistent with one another having smaller variability than the samples fabricated at 193°C. This is probably due to decreased shrinkage of the material as the temperature reaches the melting temperature of the PP. The average weight of samples fabricated at 204°C showed a slight increased with time in the mold, while the average weights of samples at 216°C showed a slight increase and then decrease with time in the mold. These changes for the 204°C and 216°C samples, however, were within the standard deviation. The pseudo-energy vs. time plot in Figure 28 showed an increase in pseudo energy for the 204°C samples as the time increased, while the samples as 216°C showed a decrease in pseudo energy as time increased. The samples at 193°C showed the most

variability with increased time in the mold. The standard deviations were large, however, making comparisons difficult.

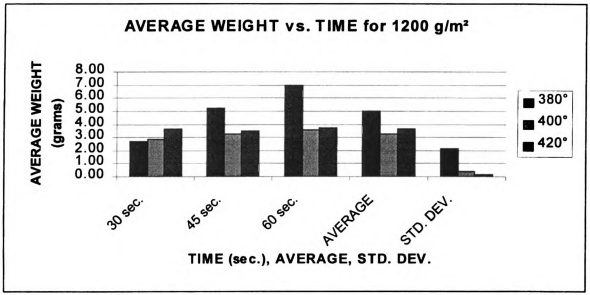

Figure 27: 1200 g/m² Average Weight vs. Time plot.

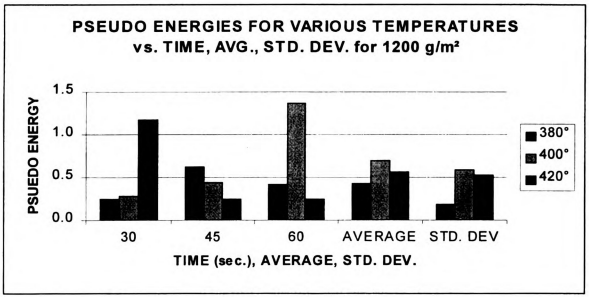

Figure 28: 1200 g/m² Pseudo-Energy vs. Time plot.

Dyna-tup Characterization of the EAM

Dyna-tup experiments were conducted on a sample of foam and a sample of EAM with backing and without backing. The foam sample was rectangular in shape and approximately four by six inches. The foam sample was impacted at a velocity of 10.4 km/hr. The impact energy was 20.4J and the total energy was around 16.3 J.

A sample EAM part that was approximately six by eight inches was impacted with backing facing the impactor. This was done to simulate HIC testing in a vehicle. The flat backing facing the impactor was ruptured during testing. The peaks, however, were deformed but not ruptured. Data showed at an impact velocity of 4.6 km/hr produced an impact energy of 20.4 J and total energy of 21.1 J. The maximum load was recorded to be around 2.7 kN.

A sample EAM part that was approximately six by eight inches was impacted without backing, thus the peaks were facing the impactor. Data in Figure 41 showed at an impact velocity of 10.4 km/hr produced an impact energy of 19.8 J and total energy of 19.9 J. The maximum load was recorded to be around 9.1 kN.

When the results of the foam impact test were compared with the sample EAM part that was impacted with backing facing the impactor, it was seen that the curves did not resemble one another since the EAM sample was damaged.

When comparing the load deflection curves of the EAM sample impacted with and without backing, the resulting graphs looked different, again due to the

sample with backing being damaged. However, the maximum load was much higher for the sample impacted without backing (9.1 kN compared to 2.7 kN).

DMA Analysis of the EAM Part I

It was also speculated that material properties varied as a function of thickness. Measurements of various locations in the EAM element cross-section were taken from previous micrographs of parts processed. In areas A and C, the thickness was 1.5-mm, area B was 1.2-mm, and the apex was .65-mm thick.

The DMA was chosen to examine the EAM, because it would be able to test relatively small samples (10 x 25 x 7 mm) as functions of both temperature and frequency. Both stiffness values and levels of energy absorption could be examined versus temperature and frequency.

Table 5 lists the parameters that were used when testing the various thicknesses in the DMA. The thicknesses correlated to the corresponding areas within the EAM element as a function of frequency. The frequencies were chosen to see how the stiffness and energy absorption varied with frequencies equivalent to velocities at impact. All samples were tested from -30° to 100°C in order to see how the material behaved in both a cold and hot environment. The samples were tested only up to 100°C to prevent melting of the sample. Samples of each thickness were tested from highest frequency to lowest frequency.

VARIOUS AUTO-STRAIN VALUES (%)			
Frequency (Hz)	1.5-mm	1.2-mm	.65-mm
150	170	170	160
15	160	140	140
1.5	150	140	140

Table 5: DMA parameters for various thickness tests.

Table 6 summarizes the initial storage modulus values and inflection temperatures. These parameters were examined to determine the sensitivity of the stiffness and T_g (material properties) to temperature and frequency. The same sample was used for all three different frequency trials.

	THICKNESS (mm)		
FREQUENCY (Hz)	**1.5**	**1.2**	**0.65**
1.5			
Initial E' (MPa)	3000	3100	4450
Inflection Temp. (°C)	5.66	3.74	1.22
15			
Initial E' (MPa)	2750	3400	4500
Inflection Temp. (°C)	6.31	8.04	6.14
150			
Initial E' (MPa)	2250	3900	4750
Inflection Temp. (°C)	14.22	11.53	7.81

Table 6: Summary of Initial Storage Modulus (E') and Inflection Temperatures (T_g) for various thicknesses and frequencies.

After this testing, four more samples at 1.2-mm thickness at 1.5 Hz, and 140% auto-strain, 2 N static load, and 45μm frequency amplitude were tested for

repeatability. Tests were run with different samples to check for repeatability. The initial storage modulus values were plotted and then compared. Table 7 gives a summary of these values. The results showed that the tests and results were repeatable having a variability around 10%.

Initial E' (MPa) for 1.2-mm Samples
2802
3320
2966
2658
3254

Table 7: Summary of Storage Modulus Values for 1.2-mm thick samples tested from -30 to 100°C at 1.5 Hz.

Results from the DMA run at three different frequencies showed that as the thickness decreased, the storage modulus values increased. This result indicated that the energy absorption characteristics would change depending on the location (and thickness) of the EAM in the cross-section. The inflection temperatures also showed some scatter of a few degrees. Since the temperatures are usually associated with intrinsic material properties, the differences detected with thickness may be due to the physical entanglements between fibers in the EAM. Sample DMA graphs for a 1.5-mm thick sample tested from -30° to 100°C at 150, 15, and 1.5 Hz are shown. The sample run at 1.5 Hz had the highest initial E' while the sample run at 150 Hz had the lowest E' value. The inflection temperatures also decreased as the frequency decreased. The data taken at 15 and 1.5 Hz showed the clearest results.

After examining the data at various frequencies, it was decided that testing should be done at 150 Hz from -30° to 100°C in order to simulate results similar to HIC testing. The total cycle time for an impact of HIC is around six milliseconds, which is equivalent to approximately 167 Hz. Samples of each thickness were tested three times. After each sample was run once in the DMA, the sample was cooled to room temperature and the DMA experiment repeated. The first group of samples that were tested at 150 Hz showed that the initial E' values and inflection temperatures changed from run to run even though the same sample was tested three times consecutively.

The initial storage modulus values are listed in Table 8 for all three thicknesses.

	1st Run	2nd Run	3RD Run
1.5-mm	4500 MPa	4750 MPa	4750 MPa
1.2-mm	4309 MPa	4569 MPa	4135 MPa
.65-mm	3999 MPa	3867 MPa	4083 MPa

Table 8: Summary of Initial Storage Modulus for various thicknesses run intermittently at 150 Hz.

This data shows that the initial storage modulus changes as a function of thickness. Since the material was allowed to cool to room temperature, the material could be experiencing residual stresses or different degrees of

crystallinity. However, the storage modulus for each sample increases as a result of the first thermal cycle and then remains the same after the second thermal cycle.

Recalling the fracture behavior of the EAM element (Figure 22), region B (1.2-mm) fractures, but regions A and C (1.5-mm) and region D (.65-mm) remained completely intact. By comparing the E' data from Table 8, the1.5-mm and 1.2-mm values correspond very closely to one another during the first run with the .65-mm values being the lowest. The 1.2-mm data has the highest E' values during the second and third runs with the 1.5-mm and .65-mm values close to one another. These trends do not reflect what we would have expected - the .65-mm samples having the highest E' values with the 1.5-mm and then 1.2-mm samples having lower values respectively. Since the .65-mm have experienced the greatest degree of compaction, we would have expected them to have the highest values with the 1.5-mm having the lowest since they are the thickest. This led us to speculate that there may be some other factors within the material affecting its performance such as voids.

A second group of samples were tested at 150 Hz for all three thicknesses, but this time the samples were run consecutively three times in a row without being cooled to room temperature for an extended period of time and then restarted. A summary of these values is shown in Table 9.

	1st Run	2nd Run	3RD Run
1.5-mm	3982 MPa	4394 MPa	4434 MPa
1.2-mm	3980 MPa	4460 MPa	4460 MPa
.65-mm	3775 MPa	4330 MPa	4441 MPa

Table 9: Summary of Initial Storage Modulus (E') for various thicknesses run consecutively at 150 Hz.

The second group of samples showed that the storage modulus values were very consistent from run to run with only the first run being lower than the other two. This was consistent for all three thicknesses, which led to the possibility that there is not a difference in the material properties (storage modulus and inflection temperature) with thickness. Since runs two and three were cooled at the same cooling rate they end up having the same crystalline structure. The first DMA run would therefore be influenced by residual and crystallization stresses, and perhaps physical entanglements between fibers.

Again, recalling the fracture behavior of the EAM element (Figure 14) - region B (1.2-mm) fractures, with regions A and C (1.5-mm) and then region D (.65-mm) intact. By comparing the E' data from Table 9, the 1.5-mm data has the highest E' values during all three runs, with the 1.2-mm and .65-mm being lower.

Therefore the way in which the samples are tested does affect the results. Samples that were allowed to completely cool between thermal runs showed different E' values in all three runs for all three thicknesses. Samples not allowed to completely cool between runs showed that only the first E' for the first run was lower than the second and third runs for all three thicknesses. It should be noted that due to these results, this "annealing" process (heating and cooling the sample) may improve energy absorption of the EAM to achieve higher E' results.

Voids and EAM

The DMA data showed that as the thickness of the samples decreased, the storage, loss and tan delta values increased, leading one to believe that the .65-mm thickness samples were stiffer due to having less voids.

To test this hypothesis, void content was measured using the ESEM. Samples were polished and mounted as described earlier and then mounted in the ESEM. By looking at representation ESEM micrographs of 1.5, 1.2, and .65-mm compressed samples (Figure 29), it appears that the 1.5-mm specimens show a larger and higher percentages of voids than the 1.2 and .65-mm samples. The 1.2-mm samples showed that voids were evident but not as large or prevalent as those seen in the 1.5-mm samples. The .65-mm samples showed very few, and very tiny voids. The fluorescent impregnated samples examined on the Olympus BH2-UMP microscope showed similar results and verified that that void content does decrease with thickness.

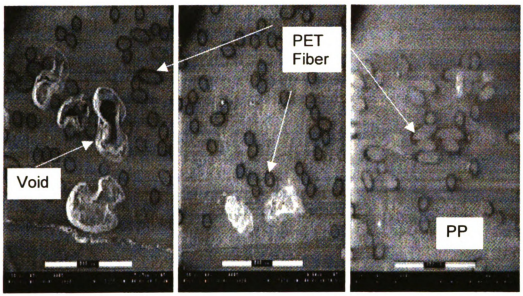

Figure 29: ESEM micrographs of 1.5, 1.2, and .65-mm samples and their void contents.

In order to try and quantify the amount of voids as a function of thickness, Archimede's Principle was used. The first group of samples was taken from the edges of the compressed sheets for all three thicknesses. This was done in order to consistently obtain samples that were 1.5, 1.2, and .65-mm in thickness, since metal shims of these thicknesses were used at the edges of the sheets. First all samples were measured in both air and hexane using a scale. The density of the sample (ρ_s) was then calculated by using the formula:

$$\rho_s = (w_a * \rho_l - w_l * \rho_a)/(w_a - w_l)$$

Where w_a is the weight of the sample in air, ρ_l is the density of hexane, w_l is the weight of the sample in hexane, ρ_a is the density of air. The void percentage was then calculated by using the formula:

Void percentage = ρ_a-ρ_s/ρ_a

The results are summarized in Table 10.

Thickness	.65-mm	1.2-mm	1.5-mm
	Voids	Voids	Voids
	0.07	0.08	0.07
	0.07	0.11	0.11
	0.08	0.16	0.08
	0.06	0.09	0.09
	0.06	0.15	0.10
	0.08	0.07	0.09
	0.09	0.08	0.10
	0.08	0.10	0.10
	0.07	0.07	0.07
	0.08	0.07	0.09
	0.11	0.10	0.10
	0.11	0.11	0.09
Average	**7.9%**	**9.8%**	**9.0%**
Std. Dev.	**1.7%**	**2.9%**	**1.4%**

Table 10: Void data of 1.5, 1.2, and .65-mm thickness samples taken from the edges of compressed sheets.

In a second experiment, the same procedure was done but samples were taken from the center of the sheets rather than the edge of the sheets. It was found that the center samples were thinner than the prescribed 1.5, 1.2, and .65-mm thicknesses. The results of this experiment are shown in Table 11.

Thickness	.65-mm	1.2-mm	1.5-mm
	Voids	Voids	Voids
	0.14	0.13	0.13
	0.13	0.13	0.13
	0.14	0.13	0.13
	0.12	0.13	0.13
	0.13	0.15	0.13
	0.12	0.13	0.12
	0.13	0.13	0.13
	0.14	0.13	0.14
	0.13	0.16	0.14
	0.14	0.13	0.12
	0.14	0.13	0.13
	0.10	0.13	0.12
Average	**13.0%**	**13.5%**	**13.0%**
Std. Dev.	**1.2%**	**1.1%**	**0.7%**

Table 11: Void data of 1.5, 1.2, and .65-mm thickness samples taken from the center of compressed sheets.

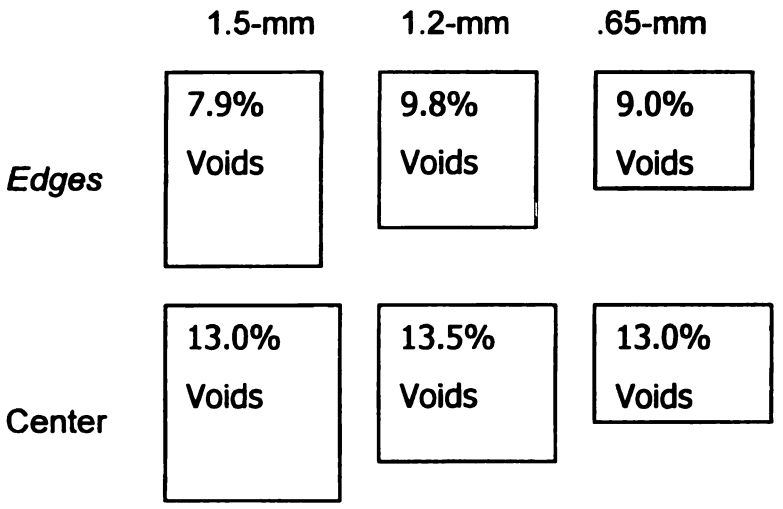

Figure 30: Summary of void data by thickness and location.

By examining both sets of void data, the results were as follows:

1. Samples taken at the edges of the sheets were more exact in the thickness dimensions due to the shims used when fabricating the sheets.
2. Samples taken from the center were much thinner in the center sections, seen mostly in the 1.2 and 1.5-mm samples due to not having shims near the center of the sheets when they were fabricated.
3. All of the void content mean and standard deviation values overlapped for all three thicknesses and contained a great deal of scatter.
4. The .65-mm samples had the most consistent void content values in both studies done: mean thickness values were pretty close compared to the 1.2 and 1.5-mm samples.

DMA Analysis of the EAM Part II

The DMA was used once again to examine fabricated EAM parts at various processing conditions. Samples needed to be tested in both the machine and cross-machine directions to see if there were differences in stiffness between the machine and cross-machine directions. The DMA was also used to determine what samples of what sections of the various processed EAM were to be tested for the high strain tensile and impact/penetration tests. Samples were fabricated on a large, scaled up mold and were processed (Figure 4) in order to get sample sections large enough for testing.

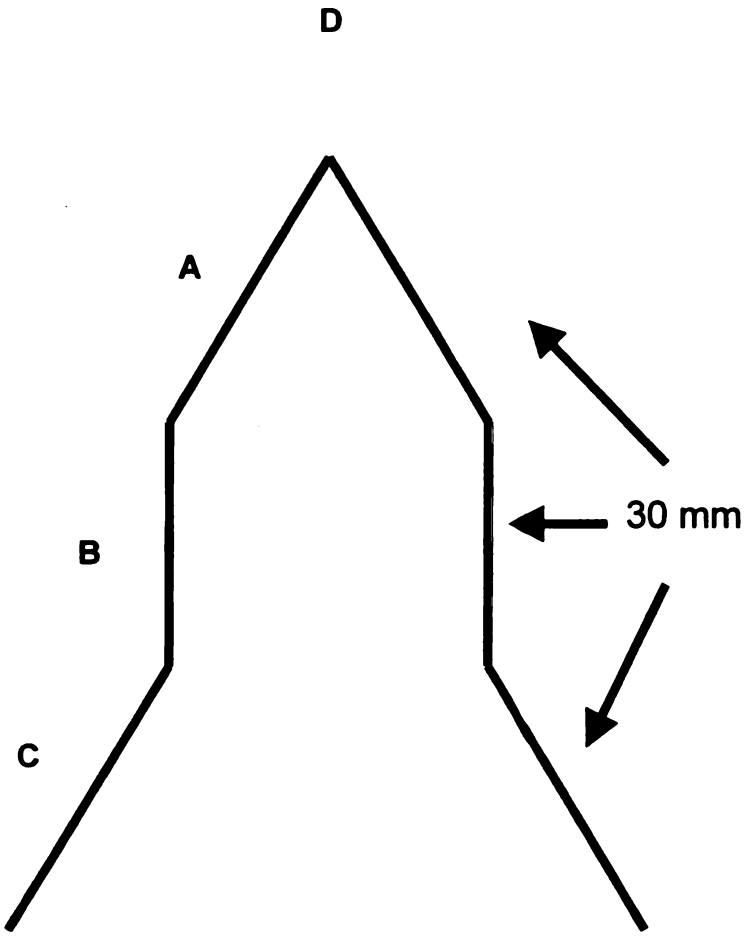

Figure 4: Drawing of enlarged EAM mold.

Parameters were selected to see how the effects of time in the heater, time in the mold, temperature, and pressure (taken here as displacement of the mold) affected the material when processed. The baseline samples processed at the plant are fabricated at 216°C for approximately 60 seconds in the heater and 45 seconds in the mold to a set displacement of 1.5-mm. The various

processing parameters dealing with times, temperatures, and pressures are shown in Table 12. They were chosen both above and below production processing parameters. Increasing the time in the heater should create more flow of the PP and therefore increase mechanical adhesion. Increasing the time in the mold would create a higher degree of consolidated material and therefore increase adhesion between PP and PET. Increasing the processing temperature should again create better flow of the PP to surround the PET fibers, thus increasing mechanical adhesion. Increasing pressure should increase the level of consolidation and reduce the presence of voids, creating a stiffer material. It should be noted that 1A, 3B, and 4A are the same sample since the processing parameters are identical.

	1 TIME 1 (HEATER sec.)	*2* TIME 2 (MOLD sec.)	*3* TEMP (°C)	*4* PRESSURE (DISP mm)
TIME 1 (HEATER sec.)	A 60* B 90 C 120	60	60	60
TIME 2 (MOLD sec.)	45	A 30 B 60	45	45
TEMP (°C)	216	216	B 216* C 227 A 238	216
PRESSURE (DISP mm)	1.5	1.5	1.5	A 1.5* B 1.25

Table 12: Processing parameters of the EAM

Three samples in both machine and cross-machine direction were tested from each region (A, B, C). Samples were approximately 12 x 11.5 x 1.5-mm and were tested at a frequency of one Hz from –100°C to 140°C. E' results of the machine and cross-machine data at –100°C are shown in Tables 13-14 respectively.

TIME 1(HEATER)			TIME 2 (MOLD)			TEMP (°C)			PRESSURE (DISP)		
Sample	Rgn	E' (MPa)	Sample	Rgn	E' (MPa)	Sample	Rgn	E' (MPa)	Sample	Rgn	E' (MPa)
1A1*	A	670.00				3B1*	A	670.00	4A1*	A	670.00
		560.00						560.00			560.00
		670.00						670.00			670.00
Average		633.33				Average		633.33	Average		633.33
	B	890.00					B	890.00		B	890.00
		660.00						660.00			660.00
		540.00						540.00			540.00
Average		696.67				Average		696.67	Average		696.67
	C	1250.00					C	1250.00		C	1250.00
		790.00						790.00			790.00
		1250.00						1250.00			1250.00
Average		1096.67				Average		1096.67	Average		1096.67
1B1	A	1100.00	2A1	A	750.00	3C1	A	860.00	4B1	A	770.00
		1020.00			770.00			960.00			1240.00
		940.00			700.00			1060.00			790.00
Average		1020.00	Average		740.00	Average		960.00	Average		933.33
	B	1190.00		B	1050.00		B	1660.00		B	1450.00
		880.00			830.00			810.00			1600.00
		880.00			980.00			1290.00			1000.00
Average		983.33	Average		953.33	Average		1253.33	Average		1350.00
	C	960.00		C	1300.00		C	1290.00		C	1900.00
		1050.00			1410.00			1160.00			1850.00
		930.00			1200.00			1670.00			1240.00
Average		980.00	Average		1303.33	Average		1373.33	Average		1663.33
1C1	A	720.00	2B1	A	1400.00	3A1	A	1150.00			
		480.00			1350.00			950.00			
		690.00			1600.00			980.00			
Average		630.00	Average		1450.00	Average		1026.67			
	B	950.00		B	1900.00		B	1230.00			
		790.00			1800.00			790.00			
		810.00			840.00			820.00			
Average		850.00	Average		1513.33	Average		946.67			
	C	1110.00		C	1700.00		C	1260.00			
		890.00			1320.00			790.00			
		680.00			1520.00			1210.00			
Average		893.33	Average		1513.33	Average		1086.67			
*NOTE: 1A = 3B = 4A, the same sample											

Table 13: E' results of DMA machine direction samples at -100°C.

TIME 1(HEATER)			TIME 2 (MOLD)			TEMP (°C)			PRESSURE (DISP)		
Sample	Rgn	E' (MPa)	Sample	Rgn	E' (MPa)	Sample	Rgn	E' (MPa)	Sample	Rgn	E' (MPa)
1A1*	A	255.0				3B1*	A	255.0	4A1*	A	255.0
		255.0						255.0			255.0
		215.0						215.0			215.0
Average		241.7				Average		241.7	Average		241.7
	B	220.0					B	220.0		B	220.0
		210.0						210.0			210.0
		210.0						210.0			210.0
Average		213.3				Average		213.3	Average		213.3
	C	350.0					C	350.0		C	350.0
		320.0						320.0			320.0
		205.0						205.0			205.0
Average		291.7				Average		291.7	Average		291.7
1B1	A	535.0	2A1	A	450.0	3C1	A	500.0	4B1	A	1300.0
		640.0			610.0			290.0			860.0
		590.0			650.0			410.0			1050.0
Average		588.3	Average		570.0	Average		400.0	Average		1070.0
	B	235.0		B	325.0		B	275.0		B	315.0
		560.0			160.0			345.0			265.0
		370.0			285.0			300.0			395.0
Average		388.3	Average		256.7	Average		306.7	Average		325.0
	C	850.0		C	380.0		C	725.0		C	1150.0
		280.0			410.0			325.0			1400.0
		525.0			505.0			840.0			520.0
Average		551.7	Average		431.7	Average		630.0	Average		1023.3
1C1	A	450.0	2B1	A	300.0	3A1	A	710.0			
		495.0			425.0			910.0			
		800.0			470.0			1250.0			
Average		581.7	Average		398.3	Average		956.7			
	B	525.0		B	250.0		B	450.0			
		280.0			455.0			370.0			
		505.0			290.0			555.0			
Average		436.7	Average		331.7	Average		458.3			
	C	1050.0		C	725.0		C	610.0			
		750.0			1000.0			540.0			
		745.0			540.0			560.0			
Average		848.3	Average		755.0	Average		570.0			
*NOTE: 1A = 3B = 4A, the same sample											

Table 14: E' DMA results in cross-machine direction at -100°C.

Since results were not very conclusive at -100°C, E' data at room temperature (approximately 20°C) were extracted from the DMA thermal graphs. The results are shown in Tables 15-16.

TIME 1(HEATER)			TIME 2 (MOLD)			TEMP (°C)			PRESSURE (DISP)		
Sample	Rgn	E' (MPa)	Sample	Rgn	E' (MPa)	Sample	Rgn	E' (MPa)	Sample	Rgn	E' (MPa)
1A1*	A	400.6				3B1*	A	400.6	4A1*	A	400.6
		333.3						333.3			333.3
		385.0						385.0			385.0
Average		373.0				Average		373.0	Average		373.0
	B	565.0					B	565.0		B	565.0
		400.0						400.0			400.0
		286.7						286.7			286.7
Average		417.2				Average		417.2	Average		417.2
	C	653.3					C	653.3		C	653.3
		475.6						475.6			475.6
		606.7						606.7			606.7
Average		578.5				Average		578.5	Average		578.5
1B1	A	660.0	2A1	A	453.3	3C1	A	515.0	4B1	A	422.2
		696.7			466.7			605.6			715.6
		511.1			377.8			613.3			453.3
Average		622.6	Average		432.6	Average		578.0	Average		530.4
	B	726.7		B	653.9		B	1050.0		B	755.6
		565.0			510.0			450.0			450.0
		505.0			627.8			772.8			533.3
Average		598.9	Average		597.2	Average		757.6	Average		579.6
	C	577.8		C	785.6		C	840.0		C	944.4
		646.7			880.0			733.3			911.1
		538.9			583.3			840.0			731.1
Average		587.8	Average		749.6	Average		804.4	Average		862.2
1C1	A	404.4	2B1	A	833.3	3A1	A	740.0			
		300.0			754.4			633.3			
		404.4			830.0			527.8			
Average		369.6	Average		805.9	Average		633.7			
	B	561.1		B	1111.0		B	762.2			
		448.9			1111.0			448.9			
		485.0			485.0			495.0			
Average		498.3	Average		902.3	Average		568.7			
	C	666.7		C	950.0		C	832.2			
		525.0			684.4			506.7			
		361.7			755.6			731.1			
Average		517.8	Average		796.7	Average		690.0			
*NOTE: 1A = 3B = 4A, the same sample											

Table 15: E' DMA results of machine direction samples at 20°C.

TIME 1(HEATER)			TIME 2 (MOLD)			TEMP (°C)			PRESSURE (DISP)		
Sample	Rgn	E' (MPa)	Sample	Rgn	E' (MPa)	Sample	Rgn	E' (MPa)	Sample	Rgn	E' (MPa)
1A1*	A	143.3				3B1*	A	143.3	4A1*	A	143.3
		146.7						146.7			146.7
		108.3						108.3			108.3
Average		132.8				Average		132.8	Average		132.8
	B	112.2					B	112.2		B	112.2
		125.2						125.2			125.2
		106.9						106.9			106.9
Average		114.8				Average		114.8	Average		114.8
	C	195.6					C	195.6		C	195.6
		171.1						171.1			171.1
		121.4						121.4			121.4
Average		162.7				Average		162.7	Average		162.7
1B1	A	313.9	2A1	A	242.5	3C1	A	287.5	4B1	A	676.7
		392.8			330 6			178.3			448.6
		317.8			377.2			235.0			562.2
Average		341.5	Average		316.8	Average		233.6	Average		562.5
	B	127.8		B	175.0		B	178.8		B	165.3
		321.4			99.2			189.6			145.0
		215.6			153.5			151.7			250.7
Average		221.6	Average		142.6	Average		173.4	Average		187.0
	C	459.2		C	233.9		C	431.1		C	613.9
		320.0			293.9			182.8			746.7
		300.3			275.0			460.0			259.7
Average		359.8	Average		267.6	Average		358.0	Average		540.1
1C1	A	252.8	2B1	A	171.1	3A1	A	382.2			
		262.5			237.5			516.7			
		415.6			266.7			770.0			
Average		310.3	Average		225.1	Average		556.3			
	B	266.4		B	125.3		B	252.8			
		164.3			233.3			233.3			
		262.8			167.9			330.0			
Average		231.2	Average		175.5	Average		272.0			
	C	557.5		C	408.9		C	350.0			
		413.3			556.1			319.4			
		400.0			265.1			323.3			
Average		456.9	Average		410.0	Average		330.9			
*NOTE: 1A = 3B = 4A, the same sample											

Table 16: E' DMA results of cross-machine direction samples at 20°C.

The results are listed according to processing parameter - time in the heater, time in the mold, temperature and pressure.

The results were then plotted for each temperature for both machine and cross-machine directions for regions A, B, and C. The results show the average and standard deviations for each of the processing groups in all three regions (Figures 31-34).

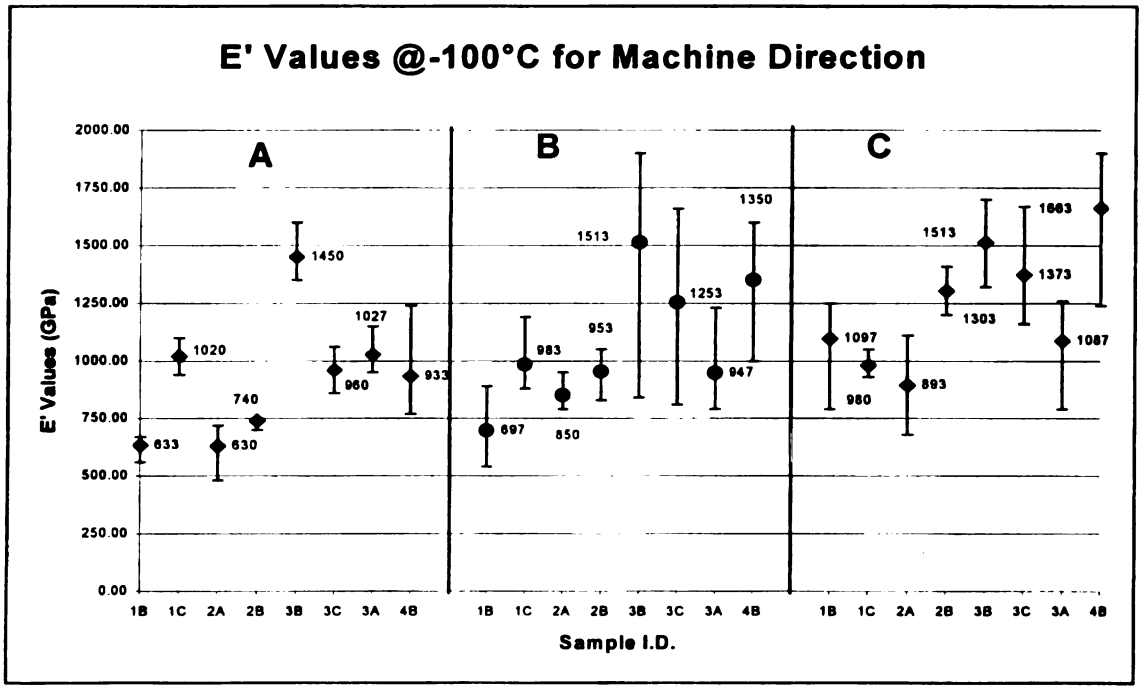

Figure 31: E' Graph for machine direction samples at -100°C.

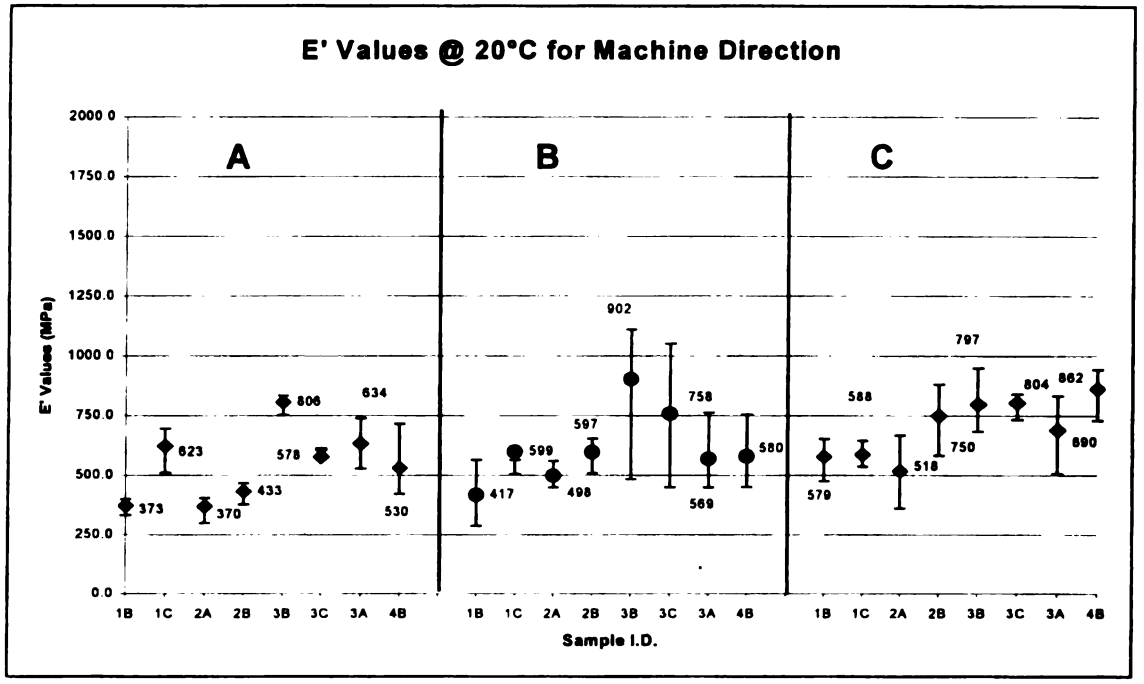

Figure 32: E' Graph for machine direction samples at 20°C.

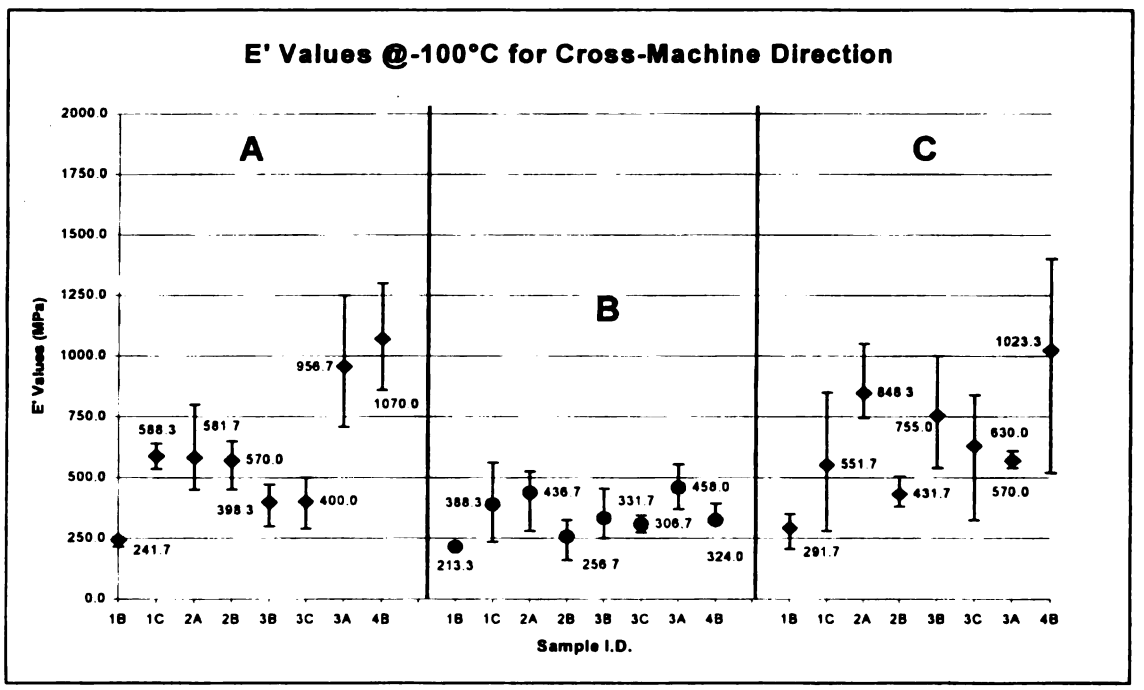

Figure 33: E' Graph for cross-machine direction samples at -100°C.

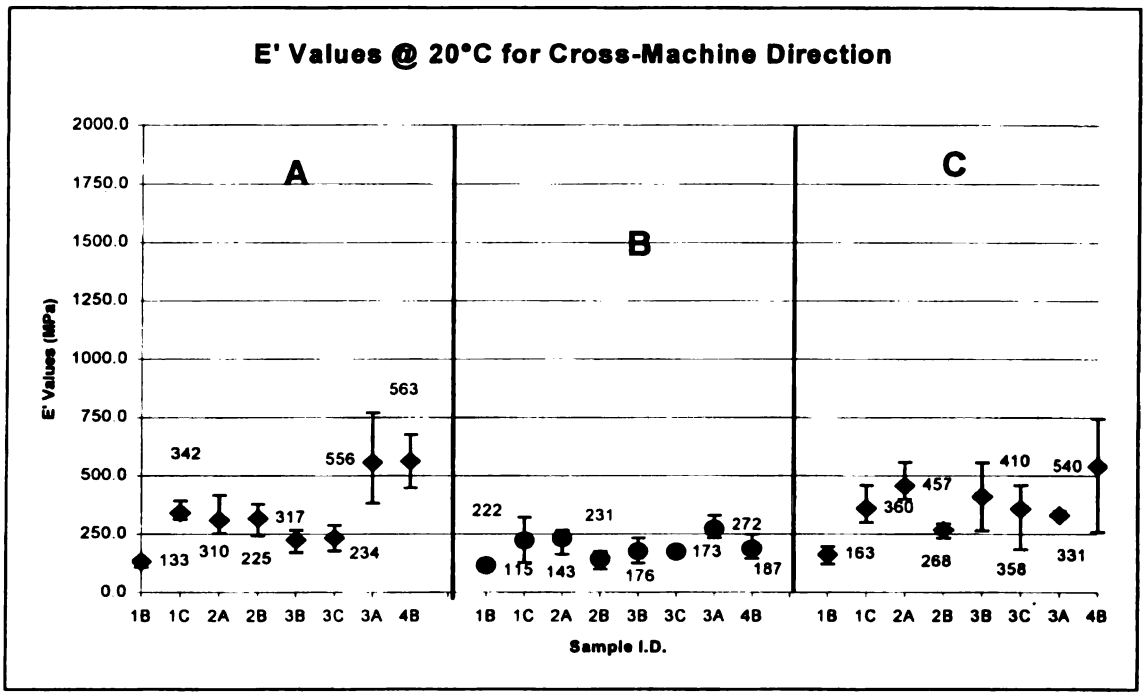

Figure 34: E' Graph for cross-machine direction samples at 20°C.

Examination of the data in Figures 54-57, show trends between the -100°C and 20°C data. The -100°C data has higher E' values than the 20°C data. The machine direction data also has higher E' values than the cross-machine data. On average, the B regions of the cross-machine data have lower E' values than the A and C regions. This correlation is not seen in the machine direction data.

To determine the effect of processing conditions, morphology, and fiber to fiber adhesion, the results were then graphed by processing condition: time in the heater, time in the mold, temperature, and pressure. Mean and sample

deviations of all three processing parameters (i.e. time in the heater - 60, 90, and 120 seconds) for cross-machine at -100°C and 20°C and machine direction at – 100°C and 20°C for all three regions A, B, and C were plotted (Figures 35-38).

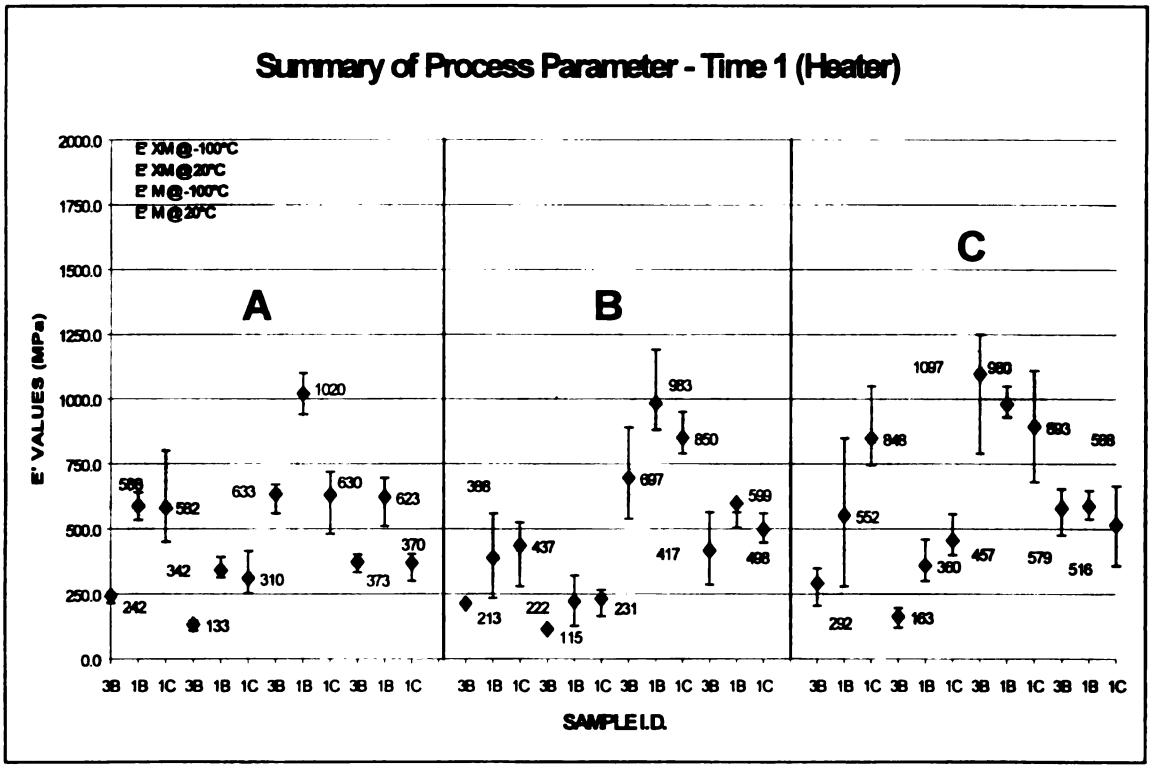

Figure 35: Initial modulus values for cross-machine and machine direction EAM as a function of time in the heater.

Figure 35 shows the results of time in the heater – 60, 90, and 120 seconds for cross-machine direction at 100°C and then 20°C and machine direction at 100°C. This is done for all three regions A, B, and C. It was assumed that as the time in the heater increased, the E' values would also increase since the PP material is allowed to flow more around the PET fibers,

increasing mechanical adhesion. This, however, was not always the case. As the time increased to 120 seconds in the heater, the E' values decreased for both cross-machine and machine directions at both –100°C and 20° for regions A, B, and C except for the cross-machine directions at both –100°C and 20°C for regions B, and C, and machine direction at –100°C in region C. By looking at Figure 58, one can also see that the E' values at -100°C have higher values than at 20°C for all three regions (A, B, C). Region C E' values at -100°C have the highest values, while E' values for region B at 20°C have the lowest values. This is due to the material being colder, and therefore having a more brittle, stiffer modulus. The standard deviations for the E' data at -100°C is also much higher than those at 20°C. By grouping all of the data in each region by temperature and direction, we see that the data at 20°C for both machine and cross-machine directions appear the same with only deviations in size due to standard deviations from the data.

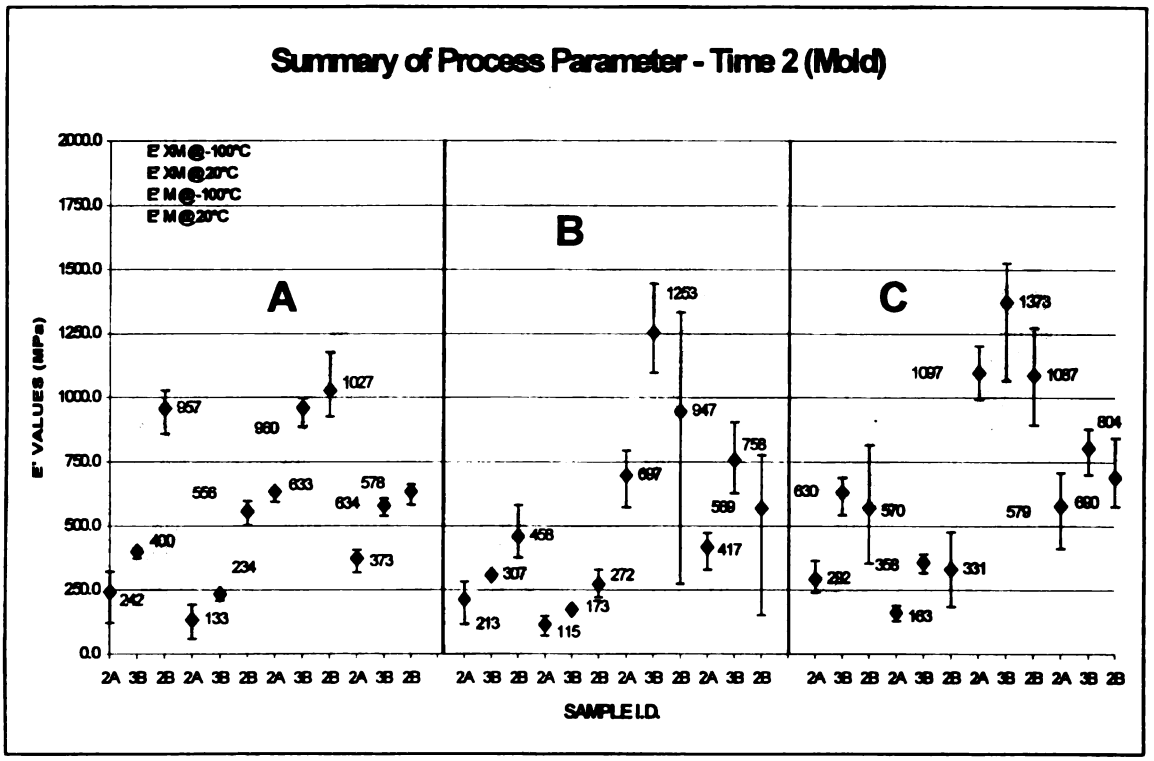

Figure 36: Initial modulus values for cross-machine and machine EAM as a function of time in the mold.

Figure 36 show the results of time in the mold – 30, 45, and 60 seconds for cross-machine at –100°C and 20°C and machine direction at –100°C and 20°C . It was assumed that as the time in the mold increased, the E' values would also increase since the longer the material was kept in the mold, the molten PP would flow to a greater degree. In region A, all E' values increase with time in the mold for both cross-machine and machine directions at –100°C and 20°C. For section B, only the cross-machine data at –100°C and 20°C showed an increase in E' values with increased time. The machine direction samples showed E' values decreasing at 60 seconds. For region C, all E' values

at -100°C have higher values than at 20°C for all three regions (A, B, C). Region C E' values at -100°C have the highest values, while E' values for region B at 20°C have the lowest values. This again is due to the material being more brittle since it is colder. The standard deviations for the E' data at -100°C is also much higher than those at 20°C, except for region B at 20°C. By grouping all of the data in each region by temperature and direction, we see that the data at 20°C for both machine and cross-machine directions, again, appear the same with only deviations in size due to standard deviations from the data.

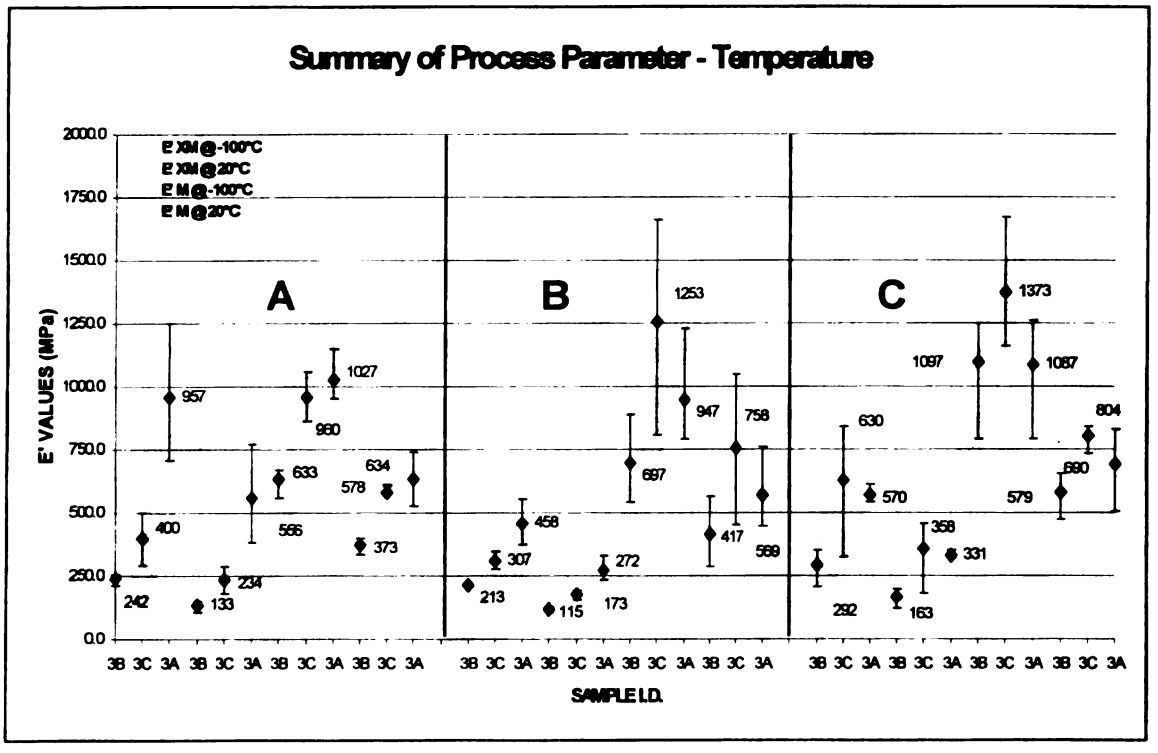

Figure 37: Initial modulus values for cross-machine and machine EAM as a function of temperature.

Figure 37 shows the results of temperature – 216°C, 227°C, and 238°C for cross-machine direction at –100°C and 20°C and machine direction at –100°C and 20°C . It was assumed that as the temperature was increased, the E' values would also increase since the PP material flows more and increases mechanical adhesion. In region A, all E' values increase with time in the mold for both cross-machine and machine directions at –100°C and 20°C. For section B, only the cross-machine data at –100°C and 20° showed an increase in E' values with increased temperature. The machine direction samples showed E' values decreasing at 238°C. For region C, all E' values decreased at 238°C. By looking at Figure 60, one can see that the E' values at -100°C have higher values than at 20°C for all three regions (A, B, C). Region C E' values at -100°C have the highest values, while E' values for region B at 20°C have the lowest values. Again this is seen due to the material being cold and thus being brittle. The standard deviations for the E' data at -100°C is also much higher than those at 20°C, except for region B at 20°C. By grouping all of the data in each region by temperature and direction, we see that the data at 20°C for both machine and cross-machine directions, again, appear the same with only deviations in size due to standard deviations from the data.

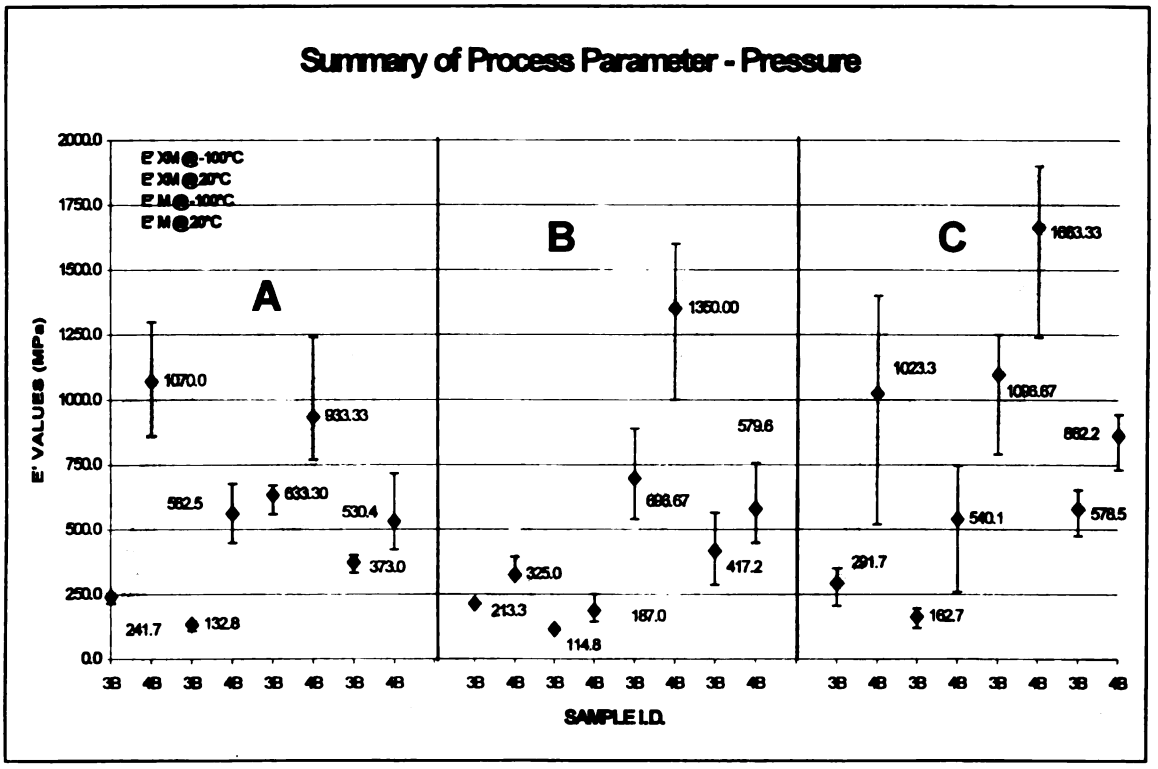

Figure 38: Initial modulus values for cross-machine and machine EAM as a function of pressure.

Figure 38 shows the effects of pressure (displacement of the mold) – 1.5-mm and 1.25 mm of displacement for cross-machine direction at –100°C and 20°C and machine direction at –100°C and 20°C. It was assumed that as the pressure increased, the E' values would also increase by diminishing the presence of voids and therefore creating a stronger material. In all cases, the E' values increased with increased pressure for all directions, temperatures, and regions. By looking at Figure 38, one can see that the E' values at -100°C have higher values than at 20°C for all three regions (A, B, C). Region C E' values at -

100°C have the highest values, while E' values for region B at 20°C have the lowest values. This due to the material being cold and thus brittle. The standard deviations for the E' data at -100°C is also much higher than those at 20°C. By grouping all of the data in each region by temperature and direction, we see that the data at 20°C for both machine and cross-machine directions, again, appear the same with only deviations in size due to standard deviations from the data.

By looking at the graphs, one can see that the data looks similar from region to region. All E' values at -100°C are higher than at 20° for all 3 regions A, B, and C. E' values at -100°C for region C seems to have the highest values overall, while region B E' values at 20°C have the lowest values. Data at -100°C have higher standard deviations than 20°C data. Regions A and C do not differ greatly in appearance to region B at 20°, except the amount of standard deviation.

The effect of increasing the time in the heater increased the scatter in the B and C regions. Increasing the time in the mold and the temperature seemed to have similar effects on the A, B, and C regions for cross-machine and machine directions at both –100°C and 20°C. It could also be due to the material being able to cool faster near the bottom of the mold. The effect of pressure increases the E' values for all directions, temperatures, and regions.

Comparability Between Small and Enlarged Samples

The E' from the B sections at 20°C were extracted and compared to E' values taken from B sections of actual EAM production samples tested at room temperature. It was speculated that the two different sizes of samples would

possibly have different material properties since they underwent different stresses while being formed in the mold. The results are shown in Table 16. Table 16 shows that E' values cover a wide range of values for both the large and small molded materials, but they are comparable, leading one to believe that the material properties are similar in both B regions for both the small production samples and the enlarged EAM samples.

E' MPa (production EAM)	E' MPa (enlarged EAM)
650	417
680	599
600	498
950	597
525	902
1250	758
	569
	580
Avg. = 775.8	**Avg. = 615.0**

Table 16: Comparison of E' values from production and enlarged EAM samples.

E" and Tan δ Comparisons

In addition to comparing the E' values, E" values were extracted from the DMA thermal graphs from the enlarged samples and plotted to see if any trends were seen compared to the high strain and impact /penetration energy results. E" represents the loss modulus or the amount of energy absorption. Looking at the E" values may be an indicator of energy absorption. The results for the E" for machine and cross-machine directions at –100°C and 20°C are shown in Figures 39-42.

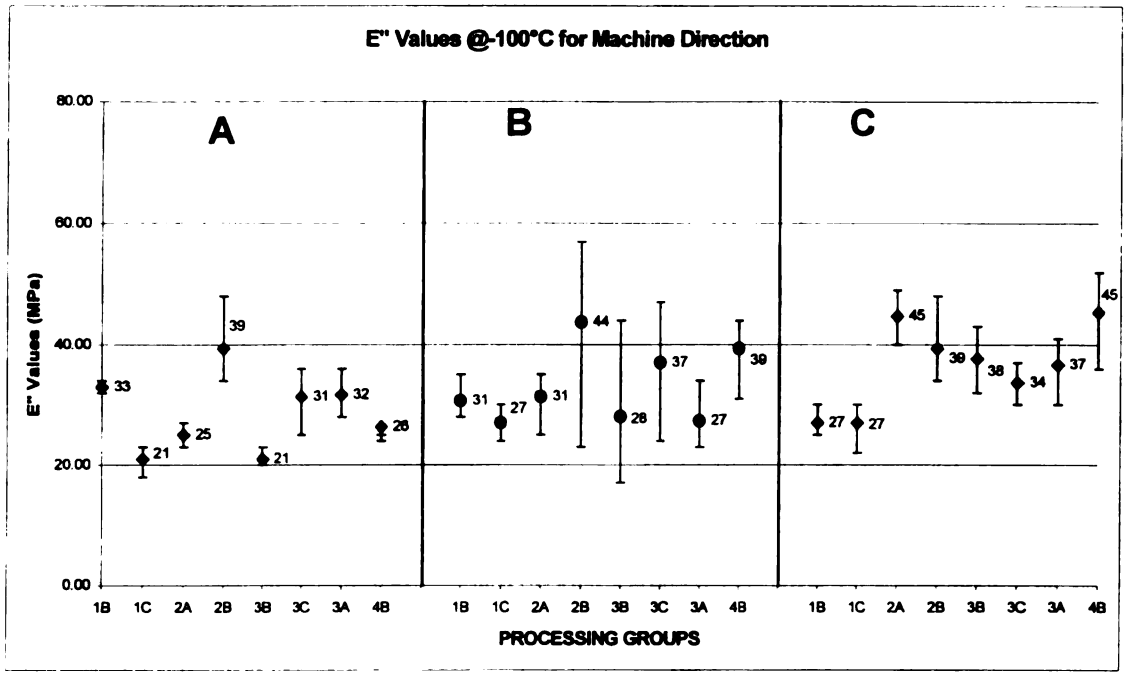

Figure 39: E" values for machine direction at –100°C.

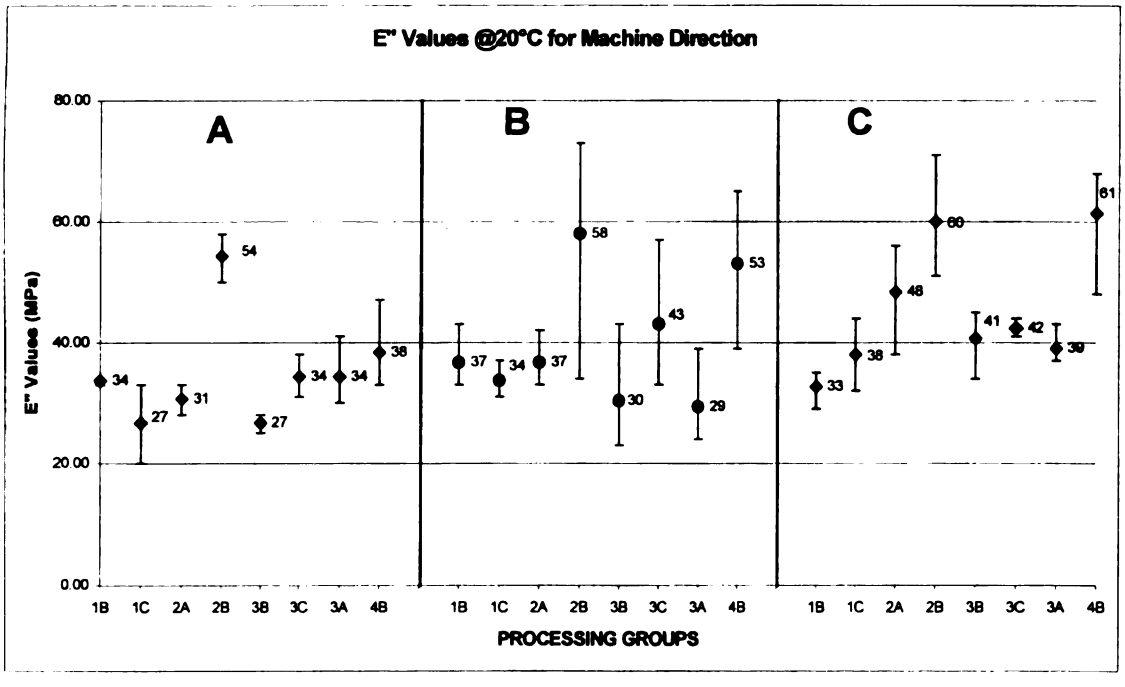

Figure 40: E" values for machine direction at 20°C.

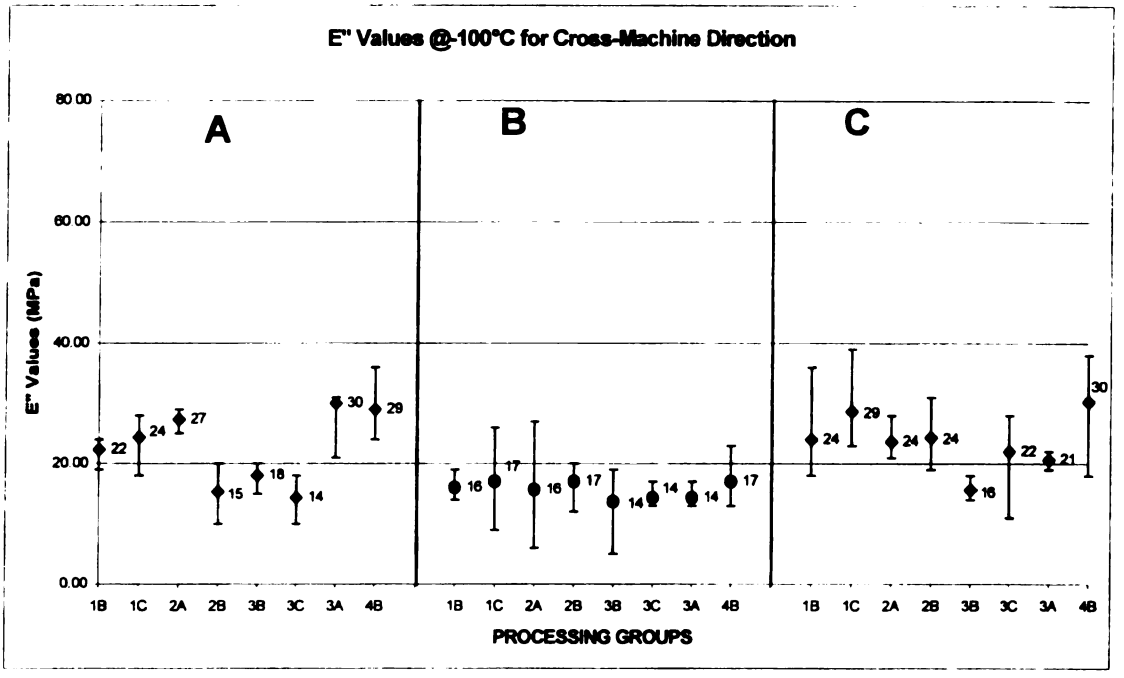

Figure 41: E" values for cross-machine direction at –100°C.

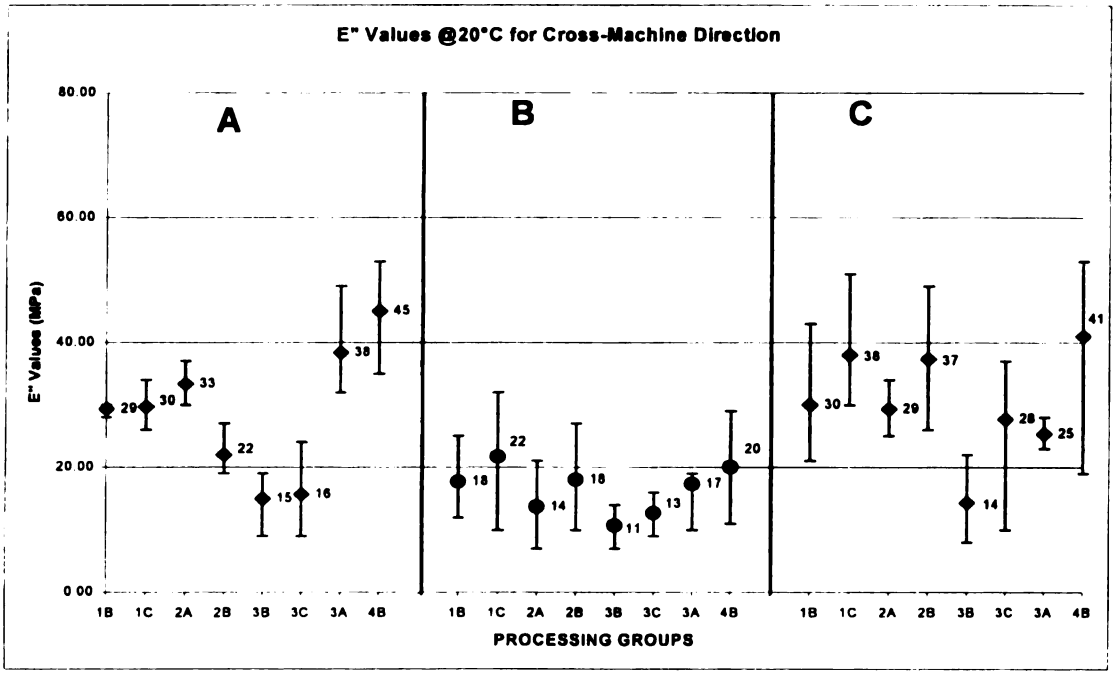

Figure 42: E" values for cross-machine direction at 20°C.

The results for the E" data showed no obvious trends or correlations between the total energy absorbed values of the high strain and impact data. However, process groups 2B and 4B in the machine direction at 20°C had the highest values. This was consistent for all three regions, indicating that energy absorption can be affected by processing.

The tan δ values for cross-machine direction at 20°C (Figure 43) were plotted and compared to the energy values for the high strain and impact data. Tan δ is the ratio of E"/E'. This ratio measures the possible energy absorption of the material normalizing the data from sample to sample. The results also did not show any firm trends or correlations, however some process parameters did have significant effects on the tan δ, and hence energy absorption.

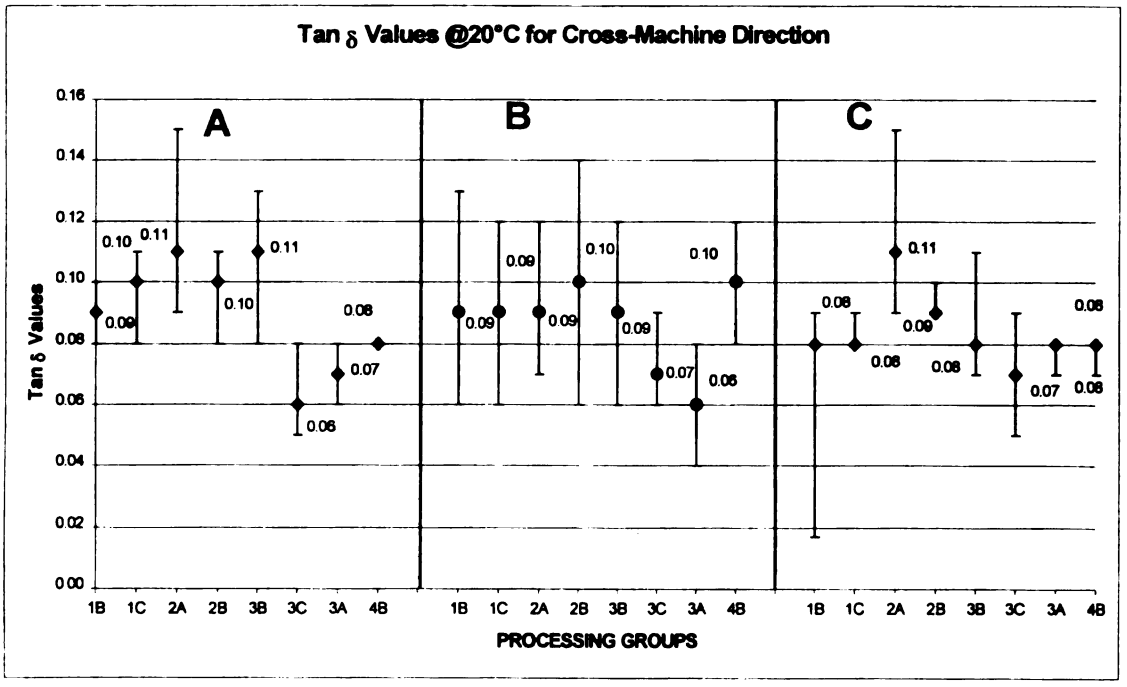

Figure 43: Tan δ values for cross-machine direction at 20°C.

Results of High Strain Tensile Tests

Five samples of each processing group (eight total) were tested at 3, 9, and 15-mph. The average values of all five samples for total energy (J), total displacement (mm), and initial force (N) are shown in Table 17.

	Sample #	Tot. Energy (J)	Tot. Disp. (mm)	Initial Force. (N)
3-mph	1B7	0.0037	2.39	67.76
9-mph	1B12	0.0013	0.79	59.53
15-mph	1B8	0.0016	0.92	67.60
3-mph	1C11	0.0038	2.55	65.26
9-mph	1C19	0.0016	0.74	76.30
15-mph	1C12	0.0016	0.99	82.04
3-mph	2A7	0.0051	2.63	81.46
9-mph	2A13	0.0014	0.90	68.41
15-mph	2A8	0.0013	0.93	79.05
3-mph	2B11	0.0032	3.37	53.41
9-mph	2B19	0.0014	0.71	65.88
15-mph	2B12	0.0011	0.96	66.61
3-mph	3B8	0.0042	2.45	68.10
9-mph	3B13	0.0010	0.80	49.29
15-mph	3B9	0.0013	1.27	74.40
3-mph	3C7	0.0058	1.78	102.05
9-mph	3C13	0.0012	0.80	58.58
15-mph	3C8	0.0015	1.16	86.83
3-mph	3A7	0.0056	3.02	92.01
9-mph	3A13	0.0014	0.74	69.85
15-mph	3A8	0.0014	1.16	83.00
3-mph	4B7	0.0040	2.29	65.30
9-mph	4B13	0.0011	0.81	55.60
15-mph	4B8	0.0012	1.17	70.90

Table 18: Results of high strain data for all 3 speeds.

Examination of the data in Table 18 shows the 3-mph samples had a higher level of energy absorption, approximately three times higher than the 9 and 15-mph samples. To evaluate how the energy varied according to parameter, the energy data was graphed according to speed and process parameter (Figures 44-47).

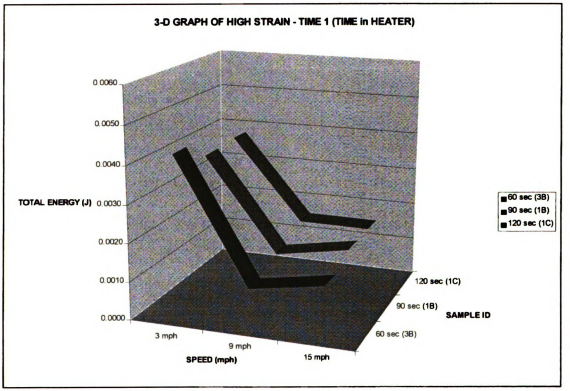

Figure 44: 3-D graph of total energy absorbed during high strain rate testing as a function of time in the heater.

Figure 44 shows the total energy values are approximately three to four times higher for the 3-mph data than the 9 and 15-mph data for all three times in

the heater. It also shows that the material tested at 3-mph are processed at 60 seconds has absorbed more total energy than at 90 and 120 seconds at 9 and 15-mph. The total energy is largest for the material processed at 120 seconds. This could be due to 60 seconds being the "cut-off" time in the heater to obtain "perfect" flow of the PP. . Longer times cause the PP to have a higher temperature and therefore a lower viscosity, causing the PP is spread too thin throughout the material and therefore reduces the level of adhesion.

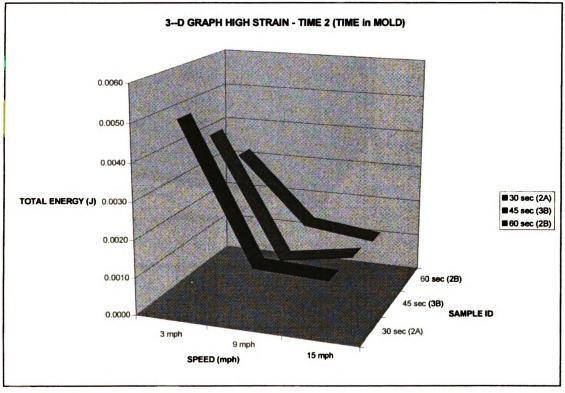

Figure 45: 3-D graph of total energy absorbed during high strain rate testing as a function of time in the mold.

Figure 45 shows the total energy at 3-mph is approximately four times higher than at 9 and 15-mph. It also shows the material processed at 30

seconds in the mold to have the highest levels of total energy at 3-mph but processing at 45 and 60 seconds results in large total energy at 9 and 15-mph. This could be due to the material being constrained too long in the mold, which then reduces the level of adhesion.

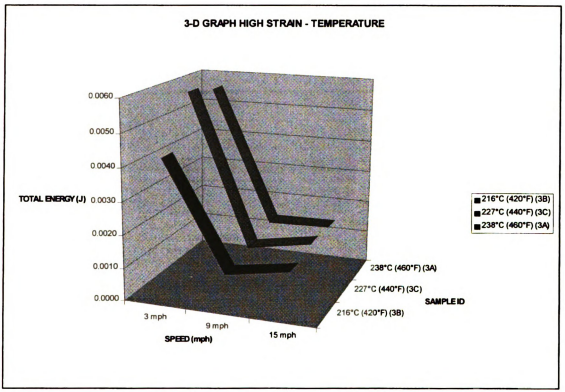

Figure 46: 3-D graph of total energy absorbed during high strain rate testing as a function of temperature.

Figure 46 shows the total energy of 3-mph data is approximately four times higher than the 9 and 15-mph data. It also shows that the material processed at 227°C and 238°C have higher similar levels of energy approximately 28% higher than at 216°C. Total energy at 9 and 15-mph is

greater at 227°C and 238°C than at 216°C. This could be due to the material reaching a sufficiently high melting temperature for more even and consistent flow of the PP over and through the PET fibers, thus leading to better mechanical

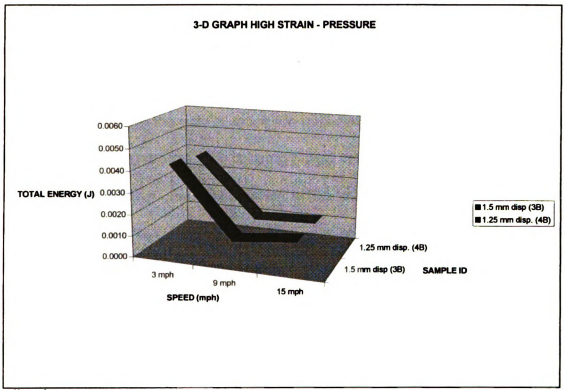

adhesion.

Figure 47: 3-D graph of total energy absorbed during high strain rate testing as a function of pressure.

Figure 47 shows that the 3-mph data is approximately four times higher than the 9 and 15-mph data. It also shows that both displacements have around the same level of energy absorption.

By looking at Figures 44-47, all energy values are considerably higher at 3-mph than at 9 and 15-mph. Materials processed at 60 seconds in the heater, 30 seconds in the mold, at 227°C or above, and at 1.5-mm of pressure all have the highest total energy values. All processing conditions tested at 3-mph showed higher total energy values than the 9 and 15-mph data. There is a change at 9-mph in which the data drops and then increases again at 15-mph. This could be due to the way in which the material behaves at slow speeds and fast speeds. Since the material is being pulled in tension, it experiences stretching and pulling. As it is stretched at the faster rate, fibers will fail in more of a brittle manner with less energy. Also, at slower speeds, sliding of the PET fibers around each other and through the PP is more likely. Perhaps 9-mph is a crossover point in which the material responds with a mixture of both kinds of speeds. This could also be due to the method of failure of the material at various speeds.

To test this hypothesis, the method of failure was then examined to try and explain the gross difference in energy absorption. Samples were evaluated visually for the amount of fiber pullout, or appearance of the samples. After looking at representative samples of all eight processing groups at all three speeds, it was seen that the 9-mph samples had very clean failure edges, with little or no tearing (Figure 48). The 15-mph samples showed very torn and "chunky" failure edges (Figure 49). The 3-mph samples exhibited a mixture of the 9 and 15-mph failure edges (Figure 50). To examine and verify this further, microscopy using an ESEM was done.

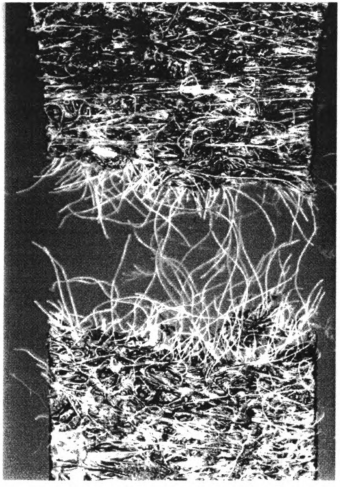

Figure 48: 9-mph clean failure edge with little tearing.

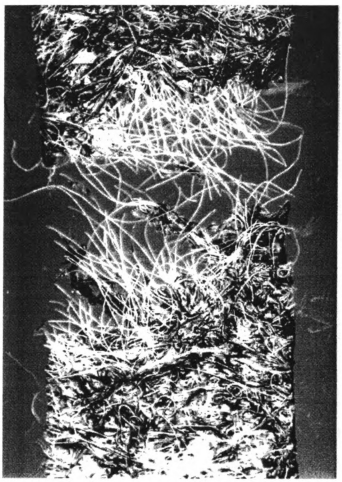

Figure 49: 15-mph torn and "chunky" failure edge.

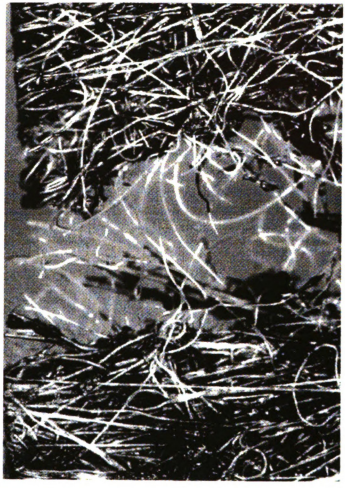

Figure 50: 3-mph with a mixture of 9 and 15-mph failure edge.

ESEM Microscopy of High Strain Tensile Samples

High strain tensile samples at 3, 9, and 15-mph were examined using an ESEM to see whether differences in the fracture surfaces would be evident from one speed to another, and also to explain why the 3-mph samples absorbed approximately three times more energy than the 9 and 15-mph samples. Gross differences from sample to sample according to different strain rates were not seen. The samples, however, were very consistent in that:

1. Clumps of PP were seen throughout all the samples (Figure 51)

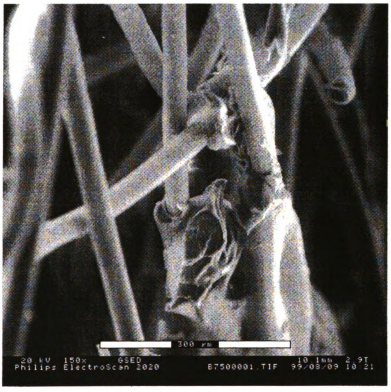

Figure 51: PP seen in clumps throughout the EAM.

2. The PET fibers failed in a brittle manner (Figure 52)

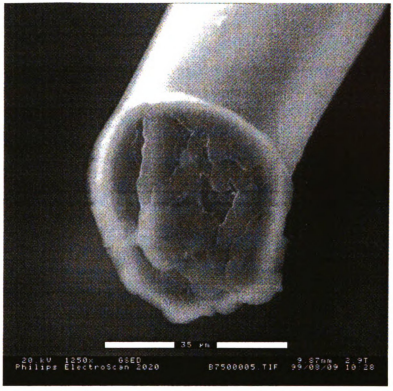

Figure 52: Fractured PET fiber surface.

3. There is both cohesive and interfacial failure of the PP, though more interfacial failure is seen (Figure 76). One can see PP does not completely adhere to or surround the PET fiber.

Figure 53: PET fiber surrounded by PP (interfacial failure).

4. Baseline samples (3B) appeared to have "stringy" PP fibrils attached to the PET fibers (Figure 54). One can see the PP fibrils attached to the PET. This is likely due to a PET fiber being pulled out of the PP.

Figure 54: PP fibrils attached to PET fibers.

5. Samples at the higher temperature (3A) seem to have more uniform PP through out the sample, with poor adhesion. Since the samples are more compressed, the PP is spread throughout more of the sample and makes the samples appear as though they have more PP than the others. The resulting adhesion, however, is still poor with PET fiber pull out.

After evaluating the samples at both low and high magnifications, a more substantive correlation between failure modes at various speeds and the amount of energy absorption could not be found.

Results of Impact/Penetration Tests

Five samples of each processing group (eight total) were impacted at 3, 9, and 15-mph. The average values of all five samples for total energy (J), total displacement (mm), and initial force (N) are shown in Table 19.

	Sample #	Tot. Energy (J)	Max. Disp. (mm)	Tot. Disp. (mm)	Max. Force (N)
3-mph	1B9	0.029	3.89	5.99	358.78
9-mph	1B10	0.056	4.24	5.52	442.25
15-mph	1B11	0.013	3.26	4.00	334.30
3-mph	1C13	0.029	4.28	6.48	407.95
9-mph	1C14	0.050	3.09	3.59	444.75
15-mph	1C15	0.014	3.67	5.21	333.90
3-mph	2A9	0.018	3.36	5.83	392.65
9-mph	2A10	0.059	3.32	4.11	489.56
15-mph	2A11	0.017	4.07	5.35	401.30
3-mph	2B17	0.021	5.51	9.30	545.10
9-mph	2B15	0.045	3.29	4.02	426.13
15-mph	2B16	0.011	4.17	5.21	304.81
3-mph	3B10	0.019	4.55	6.95	386.00
9-mph	3B11	0.058	4.84	6.24	404.38
15-mph	3B12	0.018	4.24	5.55	469.00
3-mph	3C9	0.018	4.33	5.96	336.90
9-mph	3C10	0.039	4.58	6.20	267.56
15-mph	3C11	0.015	3.11	4.18	256.19
3-mph	3A9	0.021	4.28	5.78	420.05
9-mph	3A12	0.036	3.40	6.01	421.25
15-mph	3A11	0.016	3.70	4.58	291.55
3-mph	4B9	0.017	4.03	6.09	312.20
9-mph	4B10	0.064	4.52	5.51	462.60
15-mph	4B11	0.012	3.70	4.77	289.15

Table 19: Results of impact/penetration data for all three speeds.

By looking at Table 19, the 9-mph samples had a higher level of energy absorption, approximately two to three times higher than the 3 and 15-mph samples. The 3-mph had the second highest and the 15-mph samples had the lowest. To evaluate how the energy varied according to parameter, the energy data was graphed according to speed and process parameter (Figures 55-58).

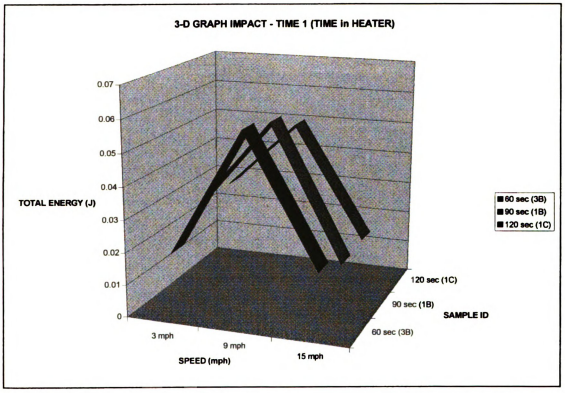

Figure 55: 3-D graph of total energy absorbed during impact testing as a function of time in the heater.

Figure 55, a 3-D graph of the amount of energy absorbed at 3, 9 and 15-mph as a function of time in the heater, shows total energy absorbed at 9-mph is approximately three to four times higher than 3 and 15-mph. It also shows

material processed at 60 seconds in the heater has the highest total energy. This again could be due to 60 seconds being the "cut-off" time in the heater to obtain "perfect" flow of the PP. Anything longer than 30 seconds causes the PP flow too much and spread in areas too thin and therefore reduces the level of adhesion.

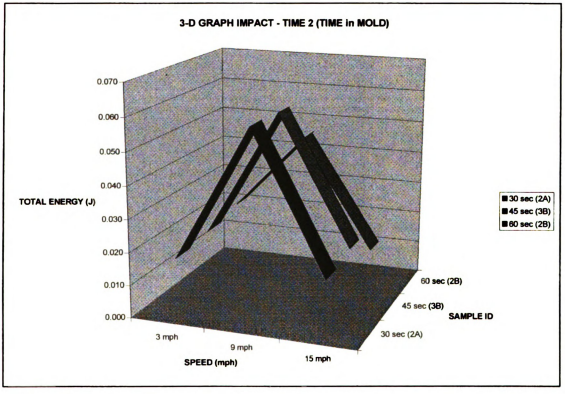

Figure 56: 3-D graph of total energy absorbed during impact testing as a function of time in the mold.

Figure 56, a 3-D graph of the amount of energy absorbed at 3, 9 and 15-mph as a function of time in the mold, shows data at 9-mph is approximately four to five times higher than at 3 and 15-mph. Again, It also shows the material

processed at 30 seconds in the mold to have the highest levels of total energy at 3-mph. This could be due to 30 seconds being the "cutoff" time in which optimum levels of molten PP adheres to PET. Anything greater than 30 seconds reduces levels of adhesion.

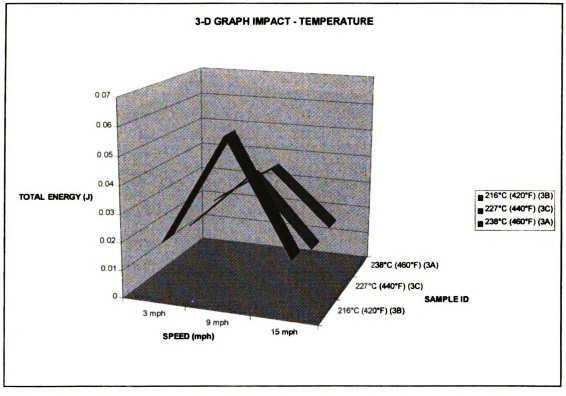

Figure 57: 3-D graph of total energy absorbed during impact testing as a function of temperature.

Figure 57, a 3-D graph of the amount of energy absorbed at 3, 9 and 15-mph as a function of temperature, shows the total energy absorbed at 9-mph approximately four times higher than at 3 and 15-mph. The total energy is

approximately 33% higher for material processed at 216°C. This could be due to 216°C being the "ideal" processing temperature for the material to achieve optimum flow and adhesion. Higher temperatures without added pressure would allow surface tension forces to contract the melt thereby reducing the effective mechanical adhesion.

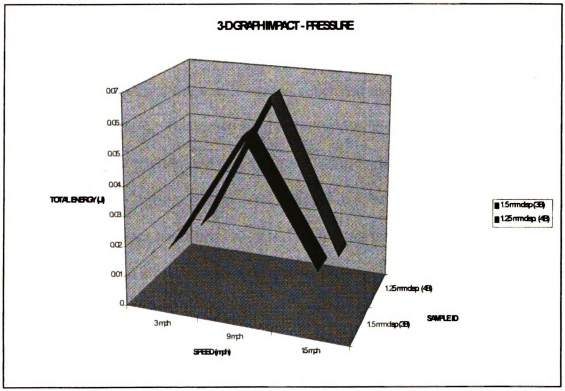

Figure 58: 3-D graph of total energy absorbed during impact testing as a function of pressure.

Figure 58, a 3-D graph of the amount of energy absorbed at 3, 9 and 15-mph as a function of pressure, shows 9-mph total energy absorbed to be approximately four to five times higher than at 3 and 15-mph. It also shows

material processed at 1.25-mm of displacement has a higher total energy at 9-mph. This could be due to more flow of the PP and thus better mechanical adhesion and fewer voids.

In Figures 55-58, all energy values are considerably higher at 9-mph than at 3 and 15-mph. At 3 and 15-mph the total energies are similar. Material processed at 60 seconds in the heater, 30 seconds in the mold, at 216°C at 1.25-mm displacement also have the highest levels of total energy. All processing conditions tested at 9-mph showed higher total energy values than the 3 and 15-mph data. There is a change at 9-mph in which the data increases and then decreases at 15-mph. This could be due to the way in which the material reacts to impacts at slow speeds and fast speed. During impact, the material experiences shear forces. When it is impacted at a faster speed, the material has less time to react and behaves in a different manner than at slower speeds. It will fail in more of a brittle manner with less energy absorption and higher force of impact. Perhaps 9-mph is a crossover point in which the material responds with a mixture of both kinds of failure modes.

To test this hypothesis, impacted material was examined to determine failure modes to explain the differences in energy absorption. Samples were evaluated visually for the amount of fiber pullout, or appearance of the samples. After looking at representative samples of all eight processing groups at all 3 speeds, it was seen that the 3-mph samples had very clean failure edges, with little or no tearing (Figure 59). The 15-mph samples showed very torn and "chunky" failure edges (Figure 60). The 9-mph samples exhibited a mixture of

the 3 and 15-mph failure edges (Figure 61). The impact failures should be different to the high strain samples since they are failing in compression and shear instead of tension during the high strain. More stretching of the PET fibers should be seen during tension testing. To examine and verify this further, microscopy using an ESEM was done.

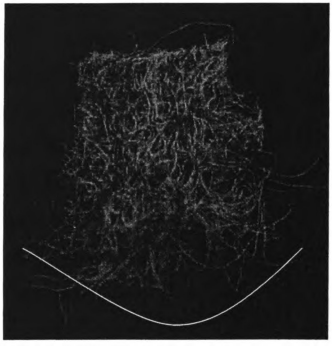

Figure 59: 3-mph impact clean impact edge.

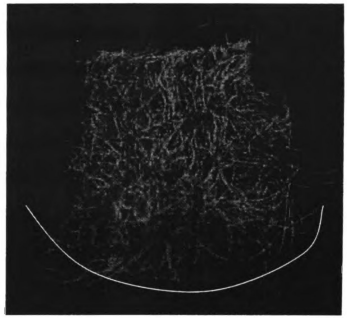

Figure 60: 15-mph impact torn and "chunky" failure edge.

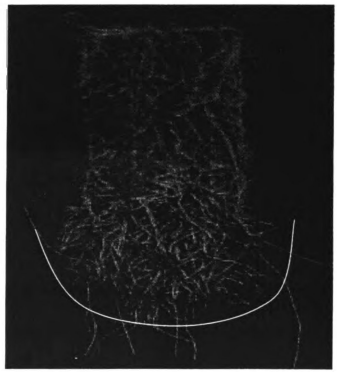

Figure 61: 9-mph mixed failure edge.

ESEM Microscopy of Impacted Samples

Impacted samples at 3, 9, and 15-mph were examined with an ESEM to determine whether gross differences in the failure mechanisms of the EAM at various speeds would be seen. Samples did not show gross differences from speed to speed, except in the way in which the PET fibers failed. Samples at 3-mph seemed to fail in a very brittle manner, with very clean surfaces (Figure 62). Samples at 15-mph showed a different type of failure with PET fiber surfaces being very jagged and torn (Figure 63). Samples at 9-mph showed a mixture of both types of failures shown in both the 3 and 15-mph samples (Figure 64).

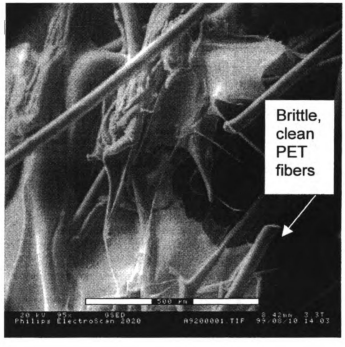

Figure 62: Brittle, clean surface failure of PET fibers at 3-mph impact.

Figure 63: Jagged and torn PET fiber failures at 15-mph impact.

Figure 64: Mixture of brittle, clean and torn and jagged PET failure at 9-mph impact.

All samples showed consistent results in that:

1. The PP stretches and breaks when it fails (Figure 65)

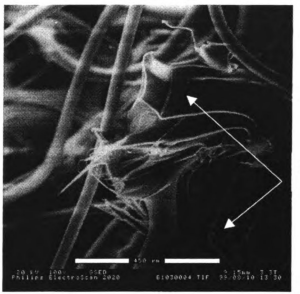

Figure 88: Stretched and broken PP throughout the EAM.

2. The PET fibers fail more in a brittle than ductile manner (Figure 66)

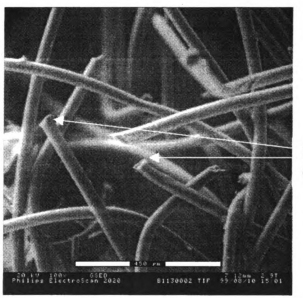

Figure 66: Brittle failure of PET fibers.

3. There is some adhesion between the PP and PET but it is very poor with the PP breaking off the PET fibers (Figure 67).

Figure 67: Breaking of PP among PET fibers.

4. PP is again found in chunks throughout the samples with the PP not being very uniform (Figure 68).

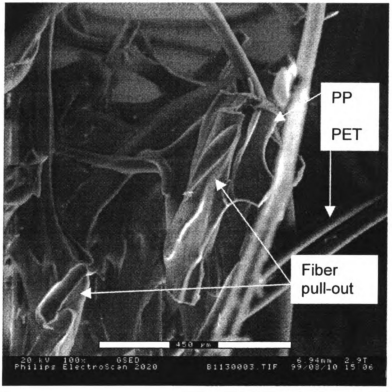

Figure 68: Non-uniform dispersion of PP, along with evidence of PET fiber pull-out of PP

5. There are large amounts of fiber pull out of the PET fibers from the PP (Figure 68).
6. The samples fail in regions of high PET concentrations and low PP concentrations (Figure 69).

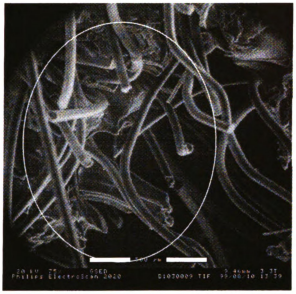

High concentration of PET fibers in fracture area of EAM

Figure 69: Failure of EAM in areas of high PET fiber concentrations.

7. There is evidence of some residual PP seen on PET fibers (Figure 70).

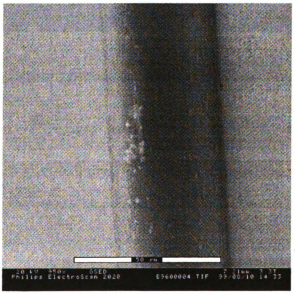

Figure 70: Remnant PP on PET fiber.

8. PP in samples processed at a higher temperature (3A) appears to be more uniformly distributed throughout the sample (Figure 71).

Figure 71: High temperature processed EAM with more uniform PP distribution.

9. High pressure samples (4B) showed the PP appears more compacted and denser (Figure 72).

Figure 72: High pressure EAM sample with more compacted and denser PP appearance.

The results of the effects of processing on the energy absorption of the EAM for both high strain and impact testing are summarized in figures 96 and 97. The results are displayed as percent changes from the baseline samples (3B) for: i) time in the heater, ii) time in the mold, iii) temperature, and iv) pressure. The baseline samples processing conditions against which the other processed samples were compared are i) 60 seconds in the heater, ii) 45 seconds in the

mold, iii) at a processing temperature of 216°C, and at iv) 1.5-mm of displacement. The graphs show trends for both high strain and impact samples.

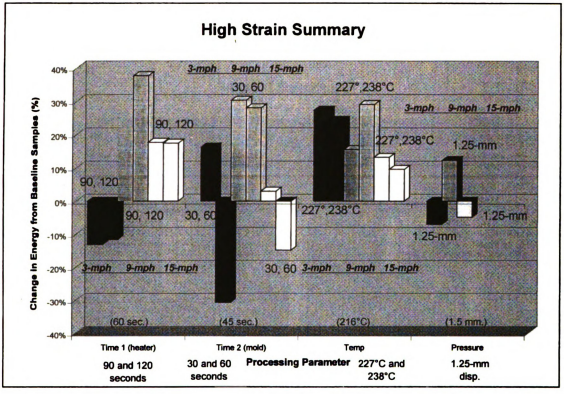

Figure 73: Summary of effects of processing parameters (Time in the heater, time in the mold, temperature and pressure) for high strain testing as percent changes from baseline samples.

The high strain data (Figure 73) shows that as time in the heater is increased, the energy absorption increases at 90 and 120 seconds for both at 9-mph and 15-mph. It also shows that decreasing the time in the mold to 30 seconds increases the energy absorption capacity of the EAM. Increasing time in the mold to 60 seconds, again decreases the energy absorption at 3 and 15-mph but increases it at 9-mph. Increasing the processing temperature to 227°

and 238°C increases the energy absorption capacity of the EAM. Increasing the pressure to 1.25-mm of displacement decreases the energy absorption at both 3 and 15-mph but increases it at 9-mph.

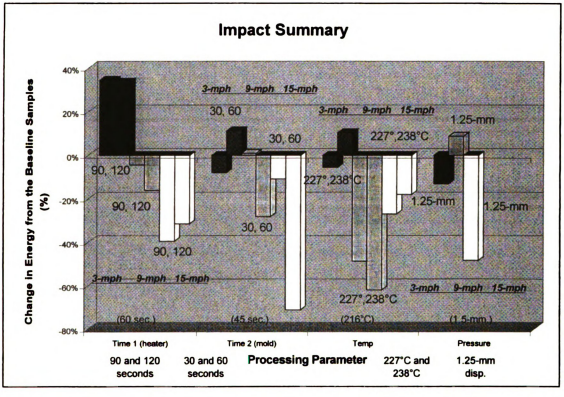

Figure 74: Summary of effects of processing parameters (Time in the heater, time in the mold, temperature and pressure) for high strain testing as percent changes from baseline samples.

The impact data (Figure 74) shows that as time in the heater is increased, the energy absorption decreases at 90 and 120 seconds for both at 9 and 15-mph and increased at 3-mph. It also shows that decreasing the time in the mold to 30 seconds decreases energy absorption for 3 and 15-mph. Increasing time in the mold to 60 seconds again increases the energy absorption at 3-mph but

decreases it at 9 and 15-mph. Increasing the processing temperature to 227°C decreases the energy absorption for all 3 speeds, but at 238°C it increases for the 3-mph data. Increasing the pressure to 1.25-mm of displacement decreases the energy absorption at both 3 and 15-mph but increases it at 9-mph.

CONCLUSIONS

1. Fluorescent impregnated samples showed that there was a relationship between the amount of fluorescent epoxy absorbed by the EAM and the level of damage seen in an element. Non-impacted samples showed little or no penetration by the fluorescent epoxy anywhere in the element, while impacted samples showed that there were large areas penetrated by fluorescent epoxy in the side wall area of the element.
   - Samples showed that there were crushing in the walls of the EAM element (region B) with the rest of the EAM element intact (regions A, C, and D).
   - Examination of these micrographs showed that failure occurs in the walls of the EAM element and not at the apex of the element which is left completely intact.
2. By evaluating micrographs, it was found that the process of fabricating the sample sheets at MSU is not representative of what is seen in the EAM when processed at the plant.
   - The process of fabricating the sheets at MSU is "too perfect," meaning it did not under go bi-axial stretching affects seen at the plant, along with shear stresses seen when the EAM is formed in the wall regions.
3. The first set of samples fabricated revealed that the mechanical properties of the EAM can change according to processes conditions.
   - This was verified by the large amount of scatter seen when examining the modulus, total energy, and pseudo energy values extracted from tensile

test data on various samples processed at different times and temperatures.

4. By comparing all three different results from the Dyna-tup testing, it was concluded that the EAM absorbs energy similar to if not better than foam to achieve the optimal energy absorption square curve.
   - Dyna-tup testing was promising, but limited since the highest impact speed that could be reached is around 12.8 km/hr.
5. Flat sample sections of EAM of 1.5, 1.2, and .65-mm thicknesses tested in the DMA at 150, 15, and 1.5 Hz showed that as the thickness decreased, the storage modulus increased. Transition temperatures were sensitive to process conditions.
   - The way in which the samples are tested does affect the results. Samples that were allowed to completely cool between thermal runs showed different E' values in all three runs for all three thicknesses. Samples not allowed to completely cool between runs showed that only the first E' for the first run was lower than the second and third runs for all three thicknesses.
   - Micrographs showed that the samples at 1.5-mm in thickness had more voids than the 1.2 and .65-mm samples. Samples were thicker near the edge and thinner in the center.
   - Examination of cross-machine and machine data in the DMA showed trends between the -100°C and 20°C data. The -100°C data has higher E' values than the 20°C data. The machine direction data also has higher E'

values than the cross-machine data. On average, the B regions of the cross-machine data have lower E' values than the A and C regions. This correlation is not seen in the machine direction data.

6. By determining the E' from DMA data of the different processed EAM groups, it was found that there were slight differences between the A, B, and C regions of the material.
   - Increasing time in the heater increased E' and the scatter in the E' data for both the B and C regions.
   - Increasing time in the mold and the processing temperature seemed to have similar effects on the E' data in all three regions of the EAM. There seems to be a difference in material properties from the material at the top region of the EAM element represented by areas A and half of B, and the bottom portion of the element represented by the bottom region of B and C.
   - Increasing the pressure increases the E' values for all directions, temperatures, and regions.
7. Evaluation and examination of the tensile failure surface of high strain tested EAM samples showed:
   - The data at 3-mph had the highest level of energy absorption for all samples. Samples processed at 60 seconds in the heater, 30 seconds in the mold, at 227°C or above, and at 1.5-mm of pressure all have the highest amount of energy absorbed.

- At nine and 15-mph the energy absorption is three to four times lower than at 3-mph.
- When examining the amount of fiber pullout, or appearance of the strained samples, the 15-mph samples showed the most fiber pullout with very jagged and "chunky" looking failure edges. The 9-mph showed the least amount of fiber pullout with very clean and little or no tears in the failure edges of the samples. The 3-mph samples showed a mixture in the amount of fiber pullout and the appearance of the failure edges of both the nine and 15-mph samples.

8. Evaluation and examination of the shear failure surface of EAM samples subjected to impact loading showed:
   - The 9-mph samples all had the highest level of energy absorption. Samples processed at 60 seconds in the heater, 30 seconds in the mold, at 216°C, and at 1.25 mm of pressure all have the highest amount of energy absorbed.
   - At three and 15-mph the energy absorption is two to three times lower than at 9-mph.
   - When examining the amount of fiber pullout, or appearance of the strained samples, the 15-mph samples showed the most fiber pullout with very jagged and "chunky" looking failure edges. The 3-mph showed the least amount of fiber pullout with very clean and little or no tears in the failure edges of the samples. The 9-mph samples showed a mixture in the

amount of fiber pullout and the appearance of the failure edges of both the nine and 15-mph samples.

- The ESEM revealed that the PET fibers fail in a very clean and brittle fashion at 3-mph, but the 15-mph fibers failed in a very jagged and torn fashion. 9-mph samples had fibers that failed in both ways.

9. Micrographs revealed that there is poor fiber to fiber adhesion of the PP and PET fibers in the EAM, primarily due to mechanical adhesion.

FUTURE RESEARCH

The following is a list of recommended experiments for the EAM:

1. Determine if there is a way to minimize the heterogeneity of the material.
2. Investigate the "annealing" process of the material – how does it affect the material and what exactly is happening to the material when it undergoes this process.
3. Determine a method to evaluate the adhesion between single PP and PET fibers.
    - Measure the adhesion between individual PP and PET fibers at different time, temperatures, and pressures in order to analyze whether or not increasing adhesion will improve energy absorption.
4. Identify why the 9-mph impact and the 3-mph high strain samples absorbed energy to a much greater extent.
5. Investigate the effect of the PP/PET ratio on energy absorption.
6. Investigate creating a uniform thickness throughout the element, especially thickening region B.

REFERENCES

1. Federal Motor Vehicle Safety Standards; Head Impact Protection (Docket 92-28, Notice 4), Federal Register, Vol. 60 (160), pp. 43032-43061, August 18, 1995.

2. Lorenzo, Luis et al., "Improving Head Impact Protection," Automotive Engineering, Vol. 104, No. 5, pp. 49-53, May 1996.

3. Syrowik, Glenn F. et al., "Energy-Absorbing Polyurethane foam to Improve Vehicle Crashworthiness," SAE Transactions: Journal of Materials and Manufacturing (USA), Vol. 104, pp. 411-420, 1995.

4. Sounik, David F. et al., "Head-Impact Testing of Polyurethane Energy-Absorbing (EA) Foams," SAE Transactions: Journal of Materials and Manufacturing (USA), Vol. 106, No. 5, pp. 211-220, 1997.

5. Porter, J.H., "Utilizing the Crushing Under Load Properties of Polypropylene and Polyethylene Honeycomb to Manage Crash Energy," SAE Transactions: Journal of Materials and Manufacturing (USA), Vol. 103, pp. 659-666, 1994.

6. Locke Deborah J. et al., "Energy-Absorbing Thermoplastics for Head-Impact Applications," SAE Transactions: Journal of Materials and Manufacturing (USA), Vol. 105, No. 5, pp. 133-137, 1996.

7. Morye, S.S. et al., "Studies in Blends of Polypropylene and Polyethylene Terepthalate," Journal of Polymer Materials, September 1996, pp. 217-221.

8. Hart, Harold, "Organic Chemistry: A Short Course," Eighth Edition, Houghton Mifflin Company, pp. 383, 397, 1991.

9. Cheung, Man Ken et al., "Mechanical and Rheological Properties of Poly(ethylene terpthalate)/Propylene Blends," Polymer International, 43, 1997, pp. 281-287.

10. Sperling, L.H., "Introduction to Physical Polymer Science," Second Edition, Lehigh University, Bethlehem, Pennsylvania, pp.322.

11. Dynatup General Research Corporation, "Dynatup Model 830-I Manual," pp. A3-1 to A3-3.

12. TA Instruments, "DMA 2980 Dynamic Mechanical Analyzer Operator's Manual," Revision C, pp. 1-4, 5-10, 1997.

13. "Dynamic Mechanical Testing," Adhesives and Sealants, Vol. 3, pp. 318-320, 1990.

14. Du Pont, DMA Handbook

15. ASM International, Engineering Materials Handbook, Volume 3 Adhesives and Sealants, pp. 318-320, 1990.

16. ASM International, Engineering Materials Handbook, Volume 2 Engineering Plastics, pp. 50-53, 1988.